J. Fluid Mech. (2021), *vol*. 915, A131, doi:10.1017/jfm.2021.127

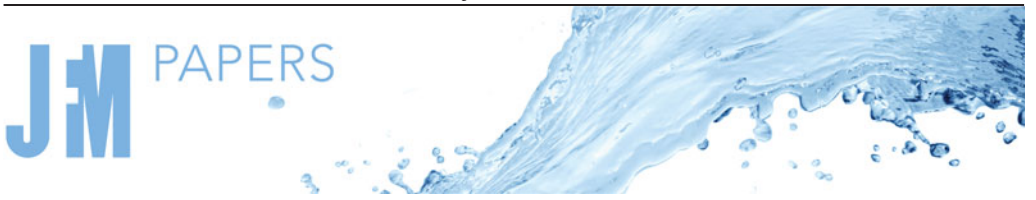

Effect of long-range Coulomb repulsion on adhesive particle agglomeration in homogeneous isotropic turbulence

Xuan Ruan[1], **Sheng Chen**[2] **and Shuiqing Li**[1],†

[1]Key Laboratory for Thermal Science and Power Engineering of Ministry of Education, Department of Energy and Power Engineering, Tsinghua University, Beijing 100084, PR China

[2]State Key Laboratory of Coal Combustion, School of Energy and Power Engineering, Huazhong University of Science and Technology, Wuhan 430074, PR China

(Received 23 August 2020; revised 28 December 2020; accepted 4 February 2021)

We conduct numerical investigations on the early-stage agglomeration of identically charged microparticles in homogeneous isotropic turbulence. The turbulent flow field is evolved by direct numerical simulation, and the adhesive discrete element method is employed to simulate particle transport and agglomerate formation. Through extensive simulations, the effect of Coulomb repulsion on collision frequency is examined. As the particle charge increases, the collision kernel, when plotted as a function of the Stokes number St, is found to change from the increasing trend to the decreasing trend. From decomposition analysis, it turns out that this monotonicity inversion is caused by the shifting of the dominant collision mechanism from preferential concentration to the sling effect. Besides, once particles contact with each other, the sticking probability is shown to solely depend on the dimensionless adhesion parameter, Ad_n, revealing the major role of interparticle adhesion in the collision process. When the effects of Coulomb repulsion and adhesion both exist, particles with moderate collision velocities are more likely to contribute to the formation of agglomerates. The structure of the agglomerates is then measured using the fractal dimension. It is found that, due to its isotropic feature, Coulomb repulsion effectively reduces the agglomeration rate but has a negligible effect on the structure of agglomerates.

Key words: multiphase flow, particle/fluid flow

1. Introduction

Particle-laden turbulent flows are ubiquitous in both natural phenomena and industrial applications. Examples include rain formation (Shaw 2003; Grabowski & Wang 2013),

† Email address for correspondence: lishuiqing@tsinghua.edu.cn

dust devils (Balme & Greeley 2006), pollutant control (Jaworek *et al.* 2018) and industrial sprays (Shrimpton & Yule 1999; Tryggvason, Scardovelli & Zaleski 2011). As a result of the strong turbulent fluctuation, suspended particles often experience frequent collisions, which directly lead to droplet coalescence (Onishi, Matsuda & Takahashi 2015; Bec *et al.* 2016), agglomerate formation (Chen, Li & Marshall 2019*a*) and charge transfer (Jin & Marshall 2017). Due to its importance and complexity, the issue of the turbulence-enhanced collision has attracted widespread attention.

The pioneering work by Saffman & Turner (1956) first revealed the essential role of turbulent collision in rain formation and formulated the collision kernel of non-inertial droplets. Then, by introducing the radial distribution function (RDF) and the relative velocity distribution, the collision kernel of inertial particles in dilute systems is expressed as (Sundaram & Collins 1997; Wang, Wexler & Zhou 2000)

$$\Gamma = 2\pi R_c^2 \cdot g(R_c) \cdot \langle |w_r| \rangle. \tag{1.1}$$

Here, R_c is the collision distance, $g(R_c)$ is the RDF at contact and w_r is the radial relative velocity. The effects of turbulence on particle collisions can then be quantified by the spatial dispersion and the radial relative velocity.

The turbulent dispersion of inertial particles has been extensively investigated. Due to the centrifugal effect, inertial particles were found to cluster in regions with low vorticity and high strain rate, which is known as preferential concentration (Maxey 1987; Squires & Eaton 1991; Eaton & Fessler 1994). Different mathematical descriptions have been employed to characterize this phenomenon, and the maximum clustering is generally observed when particle's Stokes number is around unity (Squires & Eaton 1991; Wang *et al.* 2000; Balkovsky, Falkovich & Fouxon 2001; Bec *et al.* 2007; Calzavarini *et al.* 2008*a*,*b*; Goto & Vassolicos 2008; Monchaux, Bourgoin & Cartellier 2010; Tagawa *et al.* 2012). Preferential concentration could significantly enrich the local particle concentration and thus enhance interparticle collisions (Reade & Collins 2000; Marchioli & Soldati 2002; Chun *et al.* 2005; Salazar *et al.* 2008; Saw *et al.* 2008; Jayaram *et al.* 2020). More details about particle dispersion can be found in several reviews and the references therein (Falkovich, Gawedzki & Vergassola 2001; Balachandar & Eaton 2009; Toschi & Bodenschatz 2009; Mathai, Lohse & Sun 2020). With regard to the radial relative velocity, both numerical simulations (Gustavsson & Mehlig 2014; Ireland, Bragg & Collins 2016*a*,*b*; James & Ray 2017; Bhatnagar *et al.* 2018*a*; Bhatnagar, Gustavsson & Mitra 2018*b*) and experimental studies (de Jong *et al.* 2010; Saw *et al.* 2014; Dou *et al.* 2018) have been conducted to systematically investigate the relative velocity statistics. The impacts of particle inertia and Taylor Reynolds number are further elaborated.

When particle inertia continues to increase, the sling effect or the formation of caustics can be initiated by intermittent turbulent fluctuations (Falkovich, Fouxon & Stepanov 2002; Wilkinson & Mehlig 2005; Wilkinson, Mehlig & Bezuglyy 2006). During a sling process, the particle velocity gradient detaches from the local flow field and diverges within a finite time. As a result, the particle velocity field becomes multivalued at certain positions, where particles could collide with each other at a large relative velocity (Bewley, Saw & Bodenschatz 2013). This eventually leads to a surge in collision frequency (Falkovich & Pumir 2007; Voßkuhle *et al.* 2014).

Recently, by correlating collision events with local flow characteristics, the essential role of flow structures (e.g. straining zones and intense vortical structures) in the agglomeration and deagglomeration process is unveiled. It is reported that the straining zones contribute predominantly to head-on collisions, while intense vortices could rapidly eject particles

and cause violent collisions (Perrin & Jonker 2014, 2016; Agasthya *et al.* 2019; Picardo *et al.* 2019; Chen & Li 2020).

In addition to the ideal non-interacting particles, actual particles often interact with each other through complex interactions, such as the pure elastic force (Bec, Musacchio & Ray 2013), the short-range soft repulsion (Gupta *et al.* 2018), van der Waals adhesion (Breuer & Almohammed 2015; Almohammed & Breuer 2016; Chen *et al.* 2019*a*) and electrostatic interactions (Lee *et al.* 2015). The electrostatic interactions are of interest in the present study. Particles suspended in turbulent flows usually carry electrical charge through triboelectrification or the sticking of free ions to the surface (Jones 1995; McCarty & Whitesides 2008; Pähtz, Herr,amm & Shinbrot 2010; Kolehmainen *et al.* 2018). Such systems can be found in the particle-laden flue gas in electrostatic precipitators (Jaworek *et al.* 2018), the sandstorms and dust devils on Earth or Mars (Di Renzo & Urzay 2018; Zhang & Zhou 2020) and the plumes after volcanic eruptions (Gilbert *et al.* 1991). Compared with the neutral case, the long-range electrostatic force could significantly modify the particle dynamics. For instance, the clustering of like/opposite-charged particles will be inhibited/enhanced (Karnik & Shrimpton 2012; Yao & Capecelatro 2018; Boutsikakis *et al.* 2020), and mesoscale electrical fields can be generated by the spatial separation of electrical charge (Di Renzo & Urzay 2018). By including the Coulomb force into the Fokker–Planck equation, Lu *et al.* (2010) successfully predicted the RDF for like-charged particles with finite inertia. Furthermore, for particles with negligible inertia and weak charge, by assuming that the velocities induced by turbulence and the Coulomb force could be superposed, a general model was proposed to predict charged particle behaviour in turbulence (Lu & Shaw 2015). But for larger particle inertia (Stokes number $St \geq 1$), although several studies have reported the dynamics of charged particles in turbulence, the understanding is still very limited. We thus focus on the dynamics of charged particles with $St \geq 1$.

Regarding the turbulent agglomeration of identically charged particles, however, few studies have been done on the collision frequency. Besides, the influences of particle charge on the subsequent collision and adhesion processes are less understood. In order to describe these processes, a comprehensive model is required to calculate the contact forces and torques between colliding particles. More recently, by using a direct numerical simulation (DNS)-discrete element method (DEM) coupled approach, Chen *et al.* (2019*a*) and Chen & Li (2020) investigated the agglomeration and deagglomeration of neutral particles in homogeneous isotropic turbulence and showed that the particle-scale contact interactions significantly affected the agglomeration/deagglomeration rates. However, it is still not clear how the presence of the electrostatic force will change this physical picture.

In this study, we try to address the above issues by numerically investigating the agglomeration of charged particles in turbulence. DNS is adopted to evolve the homogeneous isotropic turbulence, and the adhesive DEM is implemented to calculate particle motions. In particular, the long-range Coulomb force is calculated using the fast multipole method (FMM). The impact of Coulomb repulsion on the collision frequency between charged particles is quantified in terms of the equilibrium collision kernel. By using a decomposition analysis, we are able to identify the contributions from preferential concentration and the sling effect to the collision kernel. The modified adhesion parameter, Ad_n, defined as the ratio of interparticle adhesion to particle inertia, is then introduced to predict the post-collision behaviour. By comparing the number of sticking events, the combined effect of the Coulomb force and interparticle adhesion is elucidated. In the end, the agglomerate structure, which is described by the fractal dimension, is examined for both neutral and charged particles.

2. Methods

In this section, we introduce the numerical methods of the Eulerian–Lagrangian-based simulation. The fluid phase is evolved using DNS (§ 2.1), and the motions of suspended solid particles are computed by DEM (§ 2.2). Since various time scales are involved in the present simulation, the multiple time step algorithm is adopted to accelerate the calculation (§ 2.3). The dimensionless parameters and simulation conditions are then discussed in § 2.4.

2.1. *Gas phase: DNS*

The DNS of incompressible homogeneous and isotropic turbulence is performed using a pseudo-spectral method. The computational domain is a triply periodic cubic box with a side length $L = 2\pi$. The Cartesian grid number N^3 equals 128^3. The governing equations of the fluid phase are given by

$$\nabla \cdot \boldsymbol{u} = 0, \tag{2.1}$$

and

$$\frac{\partial \boldsymbol{u}}{\partial t} + \boldsymbol{u} \cdot \nabla \boldsymbol{u} = -\frac{1}{\rho_f}\nabla p + \nu \nabla^2 \boldsymbol{u} + \boldsymbol{f}_F + \boldsymbol{f}_P, \tag{2.2}$$

where $\boldsymbol{u}$ is the fluid velocity, p is the pressure, ρ_f and ν are the fluid density and the kinematic viscosity, respectively. The forcing term $\boldsymbol{f}_F$ is only non-zero at low wavenumbers ($|\boldsymbol{k}| \leq 5$), which maintains the turbulence at an approximately constant kinetic energy; $\boldsymbol{f}_P$ is the body force exerted by particles on the fluid phase, which can be computed by

$$\boldsymbol{f}_P(\boldsymbol{x}_i) = -\sum_{j=1}^{N_p} \boldsymbol{F}_j^F(\boldsymbol{X}_j)\delta(\boldsymbol{x}_i - \boldsymbol{X}_j). \tag{2.3}$$

Here, $\boldsymbol{x}_i$ is the position of grid node i, $\boldsymbol{F}_j^F(\boldsymbol{X}_j)$ is the fluid force acting on particle j located at $\boldsymbol{X}_j$ and $\delta(\boldsymbol{x}_i - \boldsymbol{X}_j)$ is the regularized delta function that distributes particle body force on grid nodes (Zhao, Andersson & Gillissen 2010; Dizaji & Marshall 2017).

The fluid field is initialized without particles and develops at a dimensionless fluid time step $dt_F = 0.005$. When the turbulence has reached the statistically stationary state, particles are injected into the domain for further simulations.

Table 1 lists some typical parameters describing the steady-state turbulence. u' is the fluctuation velocity, η and τ_η are Kolmogorov length and time scale, respectively. The parameter T_e is the large-eddy turnover time and Re_λ is the Taylor Reynolds number. The turbulence kinetic energy, q, and the dissipation rate, ϵ, are calculated by

$$q = \int_{k_{min}}^{k_{max}} E(k)\,\mathrm{d}k, \quad \epsilon = \int_{k_{min}}^{k_{max}} 2\nu k^2 E(k)\,\mathrm{d}k, \tag{2.4a,b}$$

where $E(k)$ is the energy spectrum.

2.2. *Solid phase: DEM*

2.2.1. *Discrete element method*

The adhesive DEM is employed to evolve both translational and rotational motions of like-charged spherical particles using Newton's second law (Li *et al.* 2011;

q	ϵ	u'	ν	η	τ_η	T_e	Re_λ
0.104	0.013	0.263	0.001	0.017	0.280	5.40	74.8

Table 1. Dimensionless flow parameters of the homogeneous isotropic turbulence.

Marshall & Li 2014). The governing equations are as follows:

$$m_i \frac{\mathrm{d}\boldsymbol{v}_i}{\mathrm{d}t} = \boldsymbol{F}_i^F + \sum_{j \neq i} \boldsymbol{F}_{ij}^C + \boldsymbol{F}_i^E, \tag{2.5a}$$

$$I_i \frac{\mathrm{d}\boldsymbol{\Omega}_i}{\mathrm{d}t} = \boldsymbol{M}_i^F + \sum_{j \neq i} \boldsymbol{M}_{ij}^C, \tag{2.5b}$$

where m_i and I_i are the particle mass and moment of inertia, $\boldsymbol{v}_i$ and $\boldsymbol{\Omega}_i$ are the translation velocity and the rotation rate; $\boldsymbol{F}_i^F$ and $\boldsymbol{M}_i^F$ are the fluid force and torque, $\boldsymbol{F}_{ij}^C$ and $\boldsymbol{M}_{ij}^C$ are the contact force and torque exerted by particle j on particle i; $\boldsymbol{F}_i^E$ is the long-range Coulomb repulsion. It is also worth noting that the influence of gravity is not included in the present study. For particles with a small Froude number, gravity modifies how particles interact with the turbulence and plays an essential role (Maxey 1987; Wang & Maxey 1993; Bec, Homann & Ray 2014; Ireland *et al.* 2016*b*; Mathai *et al.* 2016). However, in order to examine the effects of three key factors, i.e. particle inertia, the long-range Coulomb repulsion and the short-range contact force in a clear way, gravity is omitted and left for future research.

2.2.2. *Fluid force and torque on particles*

For fine solid particles suspended in the gas, the particle Reynolds number $Re_p(= |\boldsymbol{v}_i - \boldsymbol{u}|d_p/\nu)$ is much smaller than unity. Thus, the dominant fluid force and torque come from the viscous drag, which write

$$\boldsymbol{F}_i^{drag} = -3\pi\mu d_p(\boldsymbol{v}_i - \boldsymbol{u})f, \tag{2.6a}$$

$$\boldsymbol{M}_i^{drag} = -\pi\mu d_p^3(\boldsymbol{\Omega}_i - \tfrac{1}{2}\boldsymbol{\omega}), \tag{2.6b}$$

where $\boldsymbol{u}$ and $\boldsymbol{\omega} = \nabla \times \boldsymbol{u}$ are the fluid velocity and vorticity at the particle location, μ is the dynamic viscosity of the fluid and d_p is the particle diameter. The friction factor f can be calculated by the following empirical function (Di Felice 1994):

$$f = (1-\phi)^{1-\zeta}, \quad \zeta = 3.7 - 0.65exp(-\tfrac{1}{2}[1.5 - \ln(Re_p)]^2). \tag{2.7}$$

Here, ϕ is the local particle volume fraction. Apart from the viscous drag force, the Saffman lift force (Saffman 1965) and the Magnus force (Rubinov & Keller 1961) are also considered. The Saffman lift force is given by

$$\boldsymbol{F}_i^l = -2.18 m_i \frac{\rho_f}{\rho_p} \frac{(\boldsymbol{v}_i - \boldsymbol{u}) \times \boldsymbol{\omega}}{(Re_p \cdot \alpha_L)^{1/2}}, \tag{2.8}$$

where $\alpha_L = |\boldsymbol{\omega}|d_p/(2|\boldsymbol{v}_i - \boldsymbol{u}|)$, and the Magnus force is computed by

$$\boldsymbol{F}_i^m = -\frac{3}{4} m_i \frac{\rho_f}{\rho_p} \left(\frac{1}{2}\boldsymbol{\omega} - \boldsymbol{\Omega}_i\right) \times (\boldsymbol{v}_i - \boldsymbol{u}). \tag{2.9}$$

Compared to the drag force, the relative importance of the Saffman lift force and the Magnus force can be estimated by

$$F^l/F^{drag} \sim \left(\frac{\omega d_p^2}{\nu}\right)^{1/2}, \tag{2.10a}$$

$$F^m/F^{drag} \sim \frac{|\omega/2 - \Omega|d_p^2}{\nu}. \tag{2.10b}$$

In the present study, the above ratios are generally approximately $O(10^{-1})$, so the Stokes drag is the dominant fluid force. But in strong vortical structures, where ω is sufficiently large, both the Saffman lift force and the Magnus force become more significant. Besides, the Magnus force also becomes greater when oblique collisions happen. In oblique collisions, the sliding resistance (§ 2.2.4) could convert the translational energy of the particles into rotational energy, resulting in a large particle rotation rate, Ω. In such non-trivial events, the ratios could become comparable to unity. Particle behaviours will thus be significantly modulated by the Saffman lift force or the Magnus force, which adds to the uncertainty of our simulation. Since the drag force is the dominant term in most cases, the impact of other fluid forces should be limited.

2.2.3. *Long-range Coulomb repulsive force*

We apply the point-charge assumption to consider the electrostatic interaction between identically charged particles. The point charge is located at each particle centroid. The Coulomb force thus only affects the translational motion. The collision-induced charge transfer (Jin & Marshall 2017) is not incorporated in the study, so particle charge remains constant.

The Coulomb force acting on the target particle i by other source particles can be calculated by

$$\boldsymbol{F}_i^E = \sum_{j \neq i} \frac{q_i q_j (\boldsymbol{x}_i - \boldsymbol{x}_j)}{4\pi\varepsilon_0 |\boldsymbol{x}_i - \boldsymbol{x}_j|^3}, \tag{2.11}$$

where q_i is the charge of particle i, ε_0 is the vacuum permittivity.

In the triply periodic box, the domain can be regarded as an infinite space. Since the Coulomb force has a long interaction range, one key issue is how to properly realize the periodic boundary condition. In the present study, we impose image boxes in different directions to address this issue (Chen *et al.* 2016*a*; Di Renzo & Urzay 2018; Boutsikakis *et al.* 2020). After imposing N_{per} layers of image boxes around the original domain, the total number of domains equals $(2N_{per}+1)^3$. For an original source particle i located at $\boldsymbol{x}_i$, the location of its images can be given as

$$\boldsymbol{x}_i^{(l,m,n)} = \boldsymbol{x}_i + L(l\boldsymbol{i} + m\boldsymbol{j} + n\boldsymbol{k}), \quad l, m, n = -N_{per}, \ldots, N_{per}, \tag{2.12}$$

with $\boldsymbol{i}, \boldsymbol{j}, \boldsymbol{k}$ being the unit vectors along the x, y, z directions; L is the domain length. Obviously, $\boldsymbol{x}_i^{(0,0,0)} = \boldsymbol{x}_i$ is the particle location in the original box. When computing the Coulomb force, the contribution due to all the image boxes is also considered.

Equation (2.11) therefore becomes

$$\boldsymbol{F}_i^E = \sum_{j \neq i} \sum_{l,m,n=-N_{per}}^{N_{per}} \frac{q_i q_j (\boldsymbol{x}_i - \boldsymbol{x}_j^{(l,m,n)})}{4\pi\varepsilon_0 |\boldsymbol{x}_i - \boldsymbol{x}_j^{(l,m,n)}|^3}. \tag{2.13}$$

Theoretically, N_{per} should be infinite to exactly accommodate the periodic boundary condition. However, Boutsikakis *et al.* (2020) have shown that the convergence of Coulomb force is observed for $N_{per} \geq 2$. Thus, in the present study, we choose $N_{per} = 2$ as the layer number, which means the total number of domains is 125. This layer number is also adopted in the previous work by Di Renzo & Urzay (2018).

The direct summation of the pair-wise Coulomb force requires a calculation cost of $O(N_p^2)$. Therefore, we employ the FMM and reduce the calculation to $O(N_p \log N_p)$, where $N_p = 10^4$ is the number of particles in the original domain. When calculating the Coulomb force on the target particle i, the whole domain (including image domains) is first divided into a Barnes–Hut box structure (Barnes & Hut 1986). Each child box at the lowest level is a cuboid volume containing a maximum of 100 particles, FMM then uses (2.13) to directly summate the electric field generated by nearby particles while approximating the electric field from sufficiently far sources. The electrical field from a far box l at the target particle position $\boldsymbol{r}$ is approximated as

$$\boldsymbol{E}_l(\boldsymbol{r}) = \sum_m \sum_n \sum_k \frac{(-1)^{m+n+k}}{m!n!k!} I_{l.mnk} \frac{\partial^{m+n+k}}{\partial x^m \partial y^n \partial z^k} \boldsymbol{K}(\boldsymbol{r} - \boldsymbol{r}_l). \tag{2.14}$$

Here, $\boldsymbol{r}_l$ is the centroid of box l, $\boldsymbol{K}(\boldsymbol{r} - \boldsymbol{r}_l) = (\boldsymbol{r} - \boldsymbol{r}_l)/(4\pi\varepsilon_0 |\boldsymbol{r} - \boldsymbol{r}_l|^3)$ is the interaction kernel, m, n and k are indices of expansion order. The box momentum $I_{l.mnk}$ is given by

$$I_{l.mnk} = \sum_{i=1}^{N_l} Q_i (x_i - x_l)^m (y_i - y_l)^n (z_i - z_l)^k, \tag{2.15}$$

where N_l is the number of particles contained in box l, Q_i is the strength of the source i. The theoretical limit of the error in FMM is given by Salmon & Warren (1994). FMM has been successfully used in our previous works on different charged particle systems (for details, see Liu *et al.* 2010; Chen *et al.* 2016*a*; Chen, Liu & Li 2016*b*).

2.2.4. *Contact forces and torques*

When particles are in contact, the short-range contact forces and torques are taken into consideration. The normal contact force, F_{ij}^n, is determined by the Johnson–Kendall–Roberts (JKR) theory (Johnson, Kendall & Roberts 1971) together with a viscoelastic damping model. The expression is

$$F_{ij}^n = F_{ij}^{ne} + F_{ij}^{nd}, \tag{2.16a}$$

$$F_{ij}^{ne} = 4F_C \left[\left(\frac{a}{a_0} \right)^3 - \left(\frac{a}{a_0} \right)^{3/2} \right], \tag{2.16b}$$

$$F_{ij}^{nd} = \eta_N \boldsymbol{v}_{ij} \cdot \boldsymbol{n}. \tag{2.16c}$$

The first term on the right-hand side of (2.16*a*) is the normal elastic force, which is derived from the JKR model considering both van der Waals attraction and the

elastic deformation; $F_C = 3\pi\gamma R$ is the critical pull-off force; a is the radius of the contact region, and $a_0 = (9\pi\gamma R^2/E)^{1/3}$ is the equilibrium contact radius with zero load. Here, γ is the surface energy density, $R = (r_i^{-1} + r_j^{-1})^{-1}$ is the reduced radius, $E = ((1-\sigma_i^2)/E_i + (1-\sigma_j^2)/E_j)^{-1}$ is the reduced elastic modulus, E_i and σ_i are Young's modulus and Poisson's ratio of particle i, respectively. The second term is the normal dissipation force, with η_N being the normal dissipation coefficient and $\boldsymbol{v}_{ij} \cdot \boldsymbol{n}$ being the normal relative velocity (Tsuji, Tanaka & Ishida 1992).

The sliding force F_{ij}^S, the twisting torque M_{ij}^T and the rolling torque M_{ij}^R are calculated using the spring–slider–dashpot model (Sun, Battaglia & Subramaniam 2006), and are given by

$$F_{ij}^S = -min\left[k_T\left(\int_{t_0}^{t} \boldsymbol{v}_S(\tau)\cdot\boldsymbol{t}_S\,\mathrm{d}\tau\right) + \eta_T \boldsymbol{v}_S\cdot\boldsymbol{t}_S,\ F_{ij,crit}^S\right], \tag{2.17a}$$

$$M_{ij}^T = -min\left[\frac{k_T a^2}{2}\int_{t_0}^{t} \Omega_T(\tau)\,\mathrm{d}\tau + \frac{\eta_T a^2}{2}\Omega_T,\ M_{ij,crit}^T\right], \tag{2.17b}$$

$$M_{ij}^R = -min\left[4F_C\left(\frac{a}{a_0}\right)^{3/2}\left(\int_{t_0}^{t} \boldsymbol{v}_L(\tau)\,\mathrm{d}\tau\right)\cdot\boldsymbol{t}_R + \eta_R \boldsymbol{v}_L\cdot\boldsymbol{t}_R, M_{ij,crit}^R\right]. \tag{2.17c}$$

Here, $\boldsymbol{v}_S$, Ω_T, $\boldsymbol{v}_L$ are the relative sliding velocity, the twisting rate and the rolling velocity, respectively, $k_T = 8G_s a(t)$ is the tangential stiffness coefficient, $G_s = ((2-\sigma_i)/G_i + (2-\sigma_j)/G_j)^{-1}$ is the effective shear modulus with $G_i = E_i/2(1+\sigma_i)$ being the shear modulus of particle i, $\eta_T \approx \eta_N$ is the tangential viscous damping coefficient and η_R is the rolling viscous damping coefficient that depends on the restitution coefficient (Marshall 2009).

Once the critical values are exceeded, the corresponding force and torques remain unchanged while irreversible interparticle sliding, twisting and rolling occur. The critical values are listed as follows:

$$F_{ij,crit}^S = \tau_F |F_{ij}^{ne} + 2F_C|, \tag{2.18a}$$

$$M_{ij,crit}^T = \frac{3\pi}{16} a F_{ij,crit}^S, \tag{2.18b}$$

$$M_{ij,crit}^R = 4F_C\left(\frac{a}{a_0}\right)^{3/2}\theta_{crit} R, \tag{2.18c}$$

where the friction coefficient $\tau_F = 0.3$ and the critical rolling angle $\theta_{crit} = 0.02$ are chosen based on experimental measurements using atomic force microscopy (Sümer & Sitti 2008).

In the simulations, the surface energy density, $\gamma = A_H/(24\pi\delta_{min}^2)$, represents the strength of the interparticle adhesion. Here, A_H is the Hamaker coefficient, and δ_{min} is the minimum distance between two contacting surfaces. When other parameters are fixed (i.e. R, E, δ), varying γ will directly change the values of F_C, a_0 and the critical overlap $\delta_c = a_0^2/(2(6)^{1/3}R)$. The contact radius a will also change through $\delta/\delta_c = (6)^{1/3}[2(a/a_0)^2 - (4/3)(a/a_0)^{1/2}]$. Then, the contact forces and torques will be changed according to the equations introduced above. As a result, increasing γ will lead to stronger contact forces and torques.

2.3. *Multiple time step algorithm*

When particles transport and collide in turbulence, the time scale of different processes could vary by orders of magnitude. For instance, the fluid time scale is $\tau_\eta \sim O(10^{-3})s$, and the response time of a micron-size solid particle is $\tau_p = min(d_p/u, 2\rho_p r_p^2/9\mu) \sim O(10^{-5})s$. When an interparticle collision happens, the collision time scale equals $\tau_C \sim (M^2/E^2 R v_C)^{1/5} \sim O(10^{-8})s$, with v_c being the collision velocity. Directly resolving all the processes at a universal time step would be extremely time consuming. Therefore, the multiple time step algorithm is adopted to resolve different processes at different time steps so as to reduce the calculation costs (Marshall & Li 2014).

In the present study, the flow field is evolved at the dimensionless fluid time step $dt_F = 0.005$ (§ 2.1), while particle motions are updated at a smaller particle time step $dt_P = dt_F/20 = 2.5 \times 10^{-4}$. Once a particle is detected to collide with others, an ultra-fine collision time step $dt_C = dt_P/200 = 1.25 \times 10^{-6}$ is set to accurately resolve the collision process.

2.4. *Simulation conditions*

Since the parameters in the simulation are dimensionless, it is necessary to introduce the characteristic scales in the simulation. The characteristic length scale is $L_0 = 10^{-3}$ m, so the domain size $L = 2\pi$ equals 2π mm in the physical space. The density scale is $\rho_0 = 1$ kg m^{-3}, which equals the typical air density. The velocity scale $U_0 = 10$ m s^{-1} is typical for industrial applications such as turbulent-mixing agglomerators (Jaworek *et al.* 2018). This directly leads to the time scale $t_0 = L_0/U_0 = 10^{-4}$ s and the pressure scale $p_0 = \rho_0 U_0^2 = 100$ Pa. All parameters afterwards are dimensionless values, but they are still written in the original form for simplicity.

From the governing equation of particle translation, three important dimensionless parameters can be introduced. For interpretation, the dimensionless form of (2.5*a*) can be approximated by

$$m_i \frac{\mathrm{d}\boldsymbol{v}_i}{\mathrm{d}t} = 3\pi\mu d_p(\boldsymbol{u} - \boldsymbol{v}_i) + \sum_{j\neq i} 4F_C \left[\left(\frac{a}{a_0}\right)^3 - \left(\frac{a}{a_0}\right)^{3/2}\right]\boldsymbol{n}_{ij} + \sum_{j\neq i} \frac{q_i q_j \boldsymbol{r}_{ij}}{4\pi\varepsilon_0 |\boldsymbol{r}_{ij}|^3}. \quad (2.19)$$

Here, the drag force F_i^{drag} is adopted as the dominant fluid force, and the friction factor f is neglected. The normal elastic force F_{ij}^{ne} is taken as a typical measure of the contact force, where $\boldsymbol{n}_{ij}$ is the normal unit vector. It is worth noting that the particle movements are actually evolved by the governing equations introduced in § 2.2, and (2.19) is only used to derive the dimensionless parameters here. When normalized by the Kolmogorov length scale, η, and the Kolmogorov velocity scale, u_η, (2.19) can be written as

$$\frac{\mathrm{d}\boldsymbol{v}_i^*}{\mathrm{d}t^*} = \frac{1}{St}(\boldsymbol{u}^* - \boldsymbol{v}_i^*) + Ad \cdot \frac{9\eta}{2r_p} \sum_{j\neq i} \left[\left(\frac{a}{a_0}\right)^3 - \left(\frac{a}{a_0}\right)^{3/2}\right]\boldsymbol{n}_{ij} + \kappa_q \sum_{j\neq i} \frac{\boldsymbol{r}_{ij}^*}{|\boldsymbol{r}_{ij}^*|^3}. \quad (2.20)$$

Here, variables non-dimensionalized by the Kolmogorov scales are denoted by an asterisk. The particle Stokes number, St, is defined as the ratio of the particle relaxation time τ_p to the Kolmogorov time scale τ_η:

$$St = \frac{\tau_p}{\tau_\eta} = \frac{2\rho_p r_p^2}{9\mu\tau_\eta}. \quad (2.21)$$

Parameters	Values	Units
Fluid phase		
Fluid density (ρ_f)	1.0	kg m^{-3}
Domain size (L)	$2\pi \times 10^{-3}$	m
Fluid kinematic viscosity (μ)	10^{-5}	Pa · s
Solid phase		
Particle radius (r_p)	10.0	μm
Particle density (ρ_p)	12.6–75.5($St = 1$–6)	kg m^{-3}
Surface energy density (γ)	0.5–6.0($Ad = 11.1, 22.2$)	mJ m^{-2}
Charging density ($q/4\pi r_p^2$)	0–12.4($\kappa_q = 0$–1.13)	μC m^{-2}
Elastic modulus (E_p)	$(1.26–7.56) \times 10^8$	Pa
Restitution coefficient (e)	0.7	—
Poisson's ratio (σ_p)	0.33	—
Friction coefficient (τ_F)	0.3	—

Table 2. Simulation parameters.

In this study, we are dealing with fine particles suspended in turbulence, so the particle size should be smaller than or comparable to the Kolmogorov length scale, η. However, if the particle size is set very small, the particle volume fraction will be too low to obtain enough collision events. Since $\eta = 0.017$ (table 1), r_p is set to 0.01 as a balance of the above concerns and St is varied by varying the particle density ρ_p, in the second term of (2.20), the dimensionless adhesion parameter, Ad, is given by

$$Ad = \frac{\gamma}{\rho_p u_\eta^2 r_p}, \tag{2.22}$$

which is the ratio of the interparticle adhesion to particle inertia (Li & Marshall 2007). In the third term, the charge parameter, κ_q, is defined as

$$\kappa_q = \frac{3q^2}{16\pi^2 \rho_p \varepsilon_0 r_p^3 u_\eta^2 \eta}, \tag{2.23}$$

which measures the relative strength of Coulomb repulsion to that of particle inertia.

Table 2 lists the simulation parameters. The particle density, ρ_p, the surface energy density, γ, and the particle charge, q, are systematically varied to control the aforementioned dimensionless parameters (St, Ad, κ_q) and show their impacts on the particle agglomeration process. For solid surfaces, A_H is around 10^{-20} J m^{-2}, δ_{min} is in the range $0.15 - 0.40$ nm (Israelachvili 2011; Marshall & Li 2014). Thus, a typical value of γ is of the order of 10^{-1} mJ m^{-2} to 10^{1} mJ m^{-2}. The particle charging density ($0 - 12.4$ μC m^{-2}) is the common value that solid particles could obtain through field charging, diffusion charging or triboelectrification (Soh *et al.* 2012; Marshall & Li 2014).

3. Results and discussion

3.1. *Comparison of a typical collision process*

We first consider a typical collision process between two particles with/without Coulomb repulsion. In two different cases, the particle pairs are released in the turbulence with the same initial conditions and different charge parameters ($\kappa_q = 0$ and $\kappa_q = 1.13$).

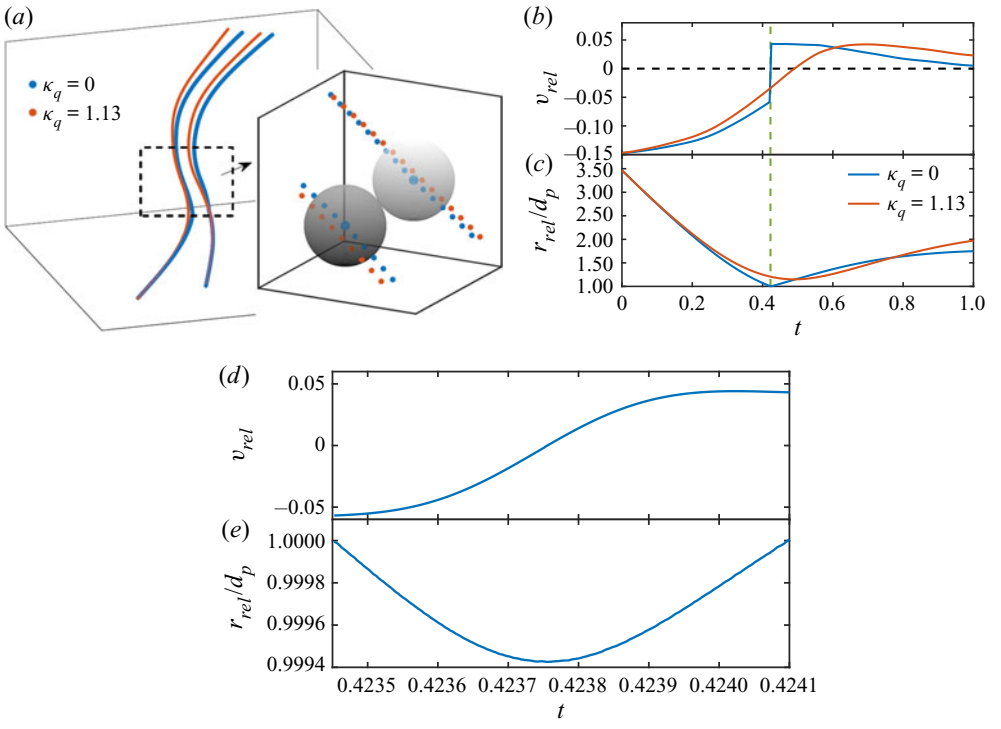

Figure 1. (*a*) Centroid trajectories of two particles in both the neutral (blue, $St = 1$, $\kappa_q = 0$) and the charged case (red, $St = 1, \kappa_q = 1.13$). In the inset, two colliding particles in the neutral case are displayed as grey spheres with their centroids enlarged. Temporal evolution of (*b*) the radial relative velocity v_{rel} and (*c*) the relative distance r_{rel} between two particles on the fluid time step dt_F. The collision moment in the neutral case is shown as the vertical green dash line, and the horizontal black dash line denotes $v_{rel} = 0$. Temporal evolution of (*d*) the radial relative velocity v_{rel} and (*e*) the normalized relative distance r_{rel}/d_p between two colliding particles on the ultra-fine collision time step dt_C. The adhesion parameter Ad equals 0.14 for both cases.

Then particle motions in both cases are evolved to show the influence of Coulomb repulsion. Figure 1(*a*) displays the trajectories of the neutral and charged particle pairs as blue and red lines. Figure 1(*b*,*c*) illustrates the corresponding temporal evolution of the radial relative velocity, $v_{rel}(= (\boldsymbol{v}_i - \boldsymbol{v}_j) \cdot (\boldsymbol{r}_i - \boldsymbol{r}_j)/|\boldsymbol{r}_i - \boldsymbol{r}_j|)$, and the interparticle distance, $r_{rel}(= |\boldsymbol{r}_i - \boldsymbol{r}_j|)$. After being released, two neutral particles have a relative inward velocity, so they start to approach each other and eventually collide (inset of figure 1*a*). In this case, due to the weak adhesive force, the colliding particles will rebound, which corresponds to the jump of the relative velocity v_{rel} from a negative value (inward) to a positive one (outward). As mentioned in § 2.3, the collision process is fully resolved on an ultra-fine collision time step dt_C and presented in figure 1(*d*,*e*). Because the fluid time step dt_F is much larger than dt_C, the rapid change of v_{rel} looks like a discontinuous jump in figure 1(*b*). For the charged particles, the trajectories coincide with the neutral ones at the beginning, but the relative velocity decreases more rapidly when particles are getting closer. Since the initial inward velocity is not large enough to overcome the Coulomb repulsion, v_{rel} reduces to zero before the particles can contact. Then v_{rel} becomes positive, and the interparticle distance starts to rise. Consequently, the collision is suppressed.

The results indicate that two competing factors determine whether a collision event will happen, i.e. the incident kinetic energy and the Coulomb repulsion. If the incident kinetic

energy is large enough to overcome the Coulomb repulsion, the approaching particles will collide. Otherwise, the collision will be prevented. Besides, our previous results have shown that the contact forces and torques will determine the sticking/rebound behaviours once particles are in contact (Chen, Li & Yang 2015). Therefore, in the following sections, both the collision frequency and the sticking probability of charged particles will be discussed to show the impact on particle agglomeration.

3.2. *Effect of Coulomb repulsion on collision frequency*

We start with the effect of Coulomb repulsion on the collision frequency. In this section, 10 000 particles are first randomly distributed in the flow field with no overlap. The initial velocity of each particle is set equal to the local fluid velocity. Then particles start to transport in the turbulence and collide with each other. Since the adhesion force is intentionally set to be weak ($Ad = 0.14$), almost all the collisions will result in a rebound. Eventually, an equilibrium state is reached, where both the spatial distribution and the collision frequency remain steady. By varying κ_q and St, the impact of the long-range Coulomb repulsion and particle inertia on the collision frequency is investigated.

The collision kernel, Γ, is employed to measure the collision frequency (Smoluchowski 1916), which is defined as

$$\Gamma = \frac{2\dot{N}_c}{n_0^2}. \tag{3.1}$$

Here, $\dot{N}_c$ is the collision rate per unit volume, $n_0 = N_p/L^3$ is the average particle number concentration. For non-inertial particles, the interparticle collision is caused by the local fluid shear rate (Saffman & Turner 1956). The corresponding collision kernel, Γ_0, equals

$$\Gamma_0 = (8\pi\epsilon/15\nu)^{1/2}(2r_p)^3. \tag{3.2}$$

The value of Γ_0 is adopted as a baseline for normalization hereafter.

The temporal evolution of the normalized collision kernel Γ/Γ_0 for different charge parameters κ_q and $St = 1$ is plotted in figure 2(*a*). In each run, Γ/Γ_0 rises in the initial stage and then fluctuates around the equilibrium value. The equilibrium value, Γ_{eq}/Γ_0, is then obtained by averaging over 12 large-eddy turnover times. Figure 2(*b*) plots the normalized equilibrium collision kernel Γ_{eq}/Γ_0 as a function of St for different κ_q. The value of Γ_{eq}/Γ_0 decreases continuously with the increase of κ_q, which results from the fact that the Coulomb force always repels approaching particles. Moreover, for neutral particles, Γ_{eq}/Γ_0 decreases monotonically as St increase, whereas for strongly charged particles, Γ_{eq}/Γ_0 rises as St increases ($\kappa_q = 0.635$ and 1.13). The reverted monotonicity suggests that the dominant collision mechanism has changed.

To further reveal the transition of the monotonicity, we adopt the decomposition analysis proposed by Voßkuhle *et al.* (2014) and Pumir & Wilkinson (2016), in which the collision enhancement is attributed to two effects: preferential concentration and the sling effect. The collision kernel is decomposed as

$$\Gamma_{eq} = \Gamma_{pref} + \Gamma_{sling}. \tag{3.3}$$

Here, Γ_{pref} and Γ_{sling} are the contributions from preferential concentration and the sling effect, respectively.

Due to preferential concentration, particles tend to cluster in the straining regions outside the vortical structures. Without the sling effect, the particle velocity field is single valued, so the trajectories of nearby particles are approximately parallel (Bewley

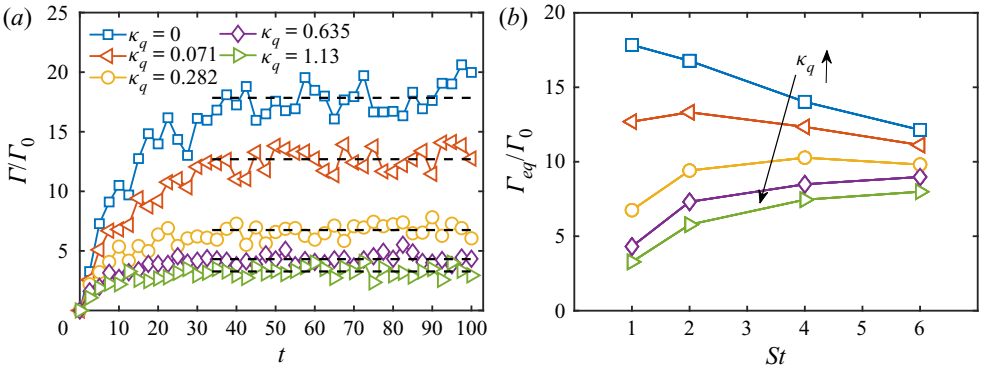

Figure 2. (*a*) Temporal evolution of the normalized collision kernel Γ/Γ_0 for different charge parameters κ_q with $St = 1$. The equilibrium values are displayed as horizontal black dash lines. (*b*) The equilibrium collision kernel as a function of Stokes number St for different charge parameter κ_q. The adhesion parameter Ad equals 0.14 for all cases. The legend in (*a*) also applies to (*b*).

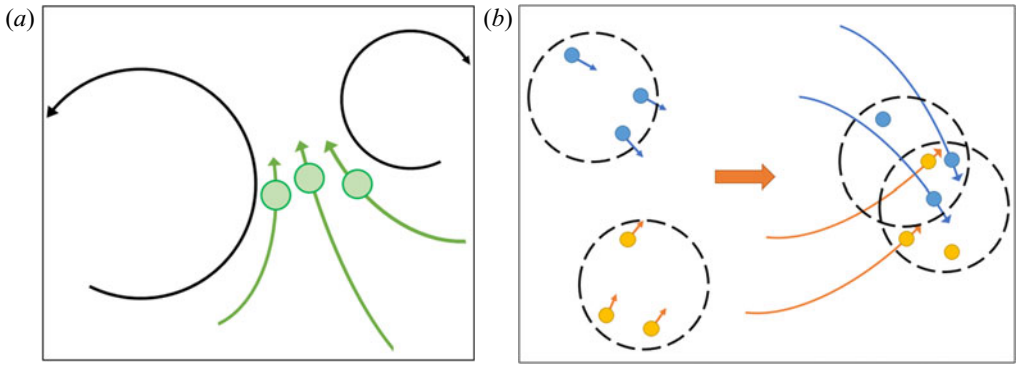

Figure 3. Schematics of (*a*) preferential concentration and (*b*) the sling effect.

et al. 2013). In this case, collisions happen when adjacent particles are moving along their trajectories and collide with each other due to the local fluid shear rate (figure 3*a*). According to Voßkuhle *et al.* (2014), the clustering of particles in straining zones only has minor impacts on their relative velocity, so the collision kernel between clustering particles can still be given by Γ_0. As a result, Γ_{pref} can be computed by

$$\Gamma_{pref} = \Gamma_0 \cdot g(d_p), \tag{3.4}$$

where $g(d_p)$ is the RDF at contact.

When encountering intermittent fluctuations, particle clouds from different regions could quickly interpenetrate each other, resulting in the crossing of particle trajectories (figure 3*b*). The formation of such singularities in the particle velocity field (or the caustics) is related to large relative velocity and further enhances interparticle collisions. The contribution of the sling effect, Γ_{sling}, is then computed by subtracting Γ_{pref} from Γ_{eq}.

To measure Γ_{pref}/Γ_0, we calculate the RDF at contact $g(d_p)$ for each case. Figure 4(*a*) displays $\Gamma_{pref}/\Gamma_0 (= g(d_p))$ as a function of St for different charge parameter κ_q. For the neutral case, Γ_{pref}/Γ_0 shows a monotonically decreasing trend on St and experiences its peak when St is around unity, which is consistent with previous DNS results (Wang *et al.* 2000). For charged particles, the presence of the repulsive Coulomb force is

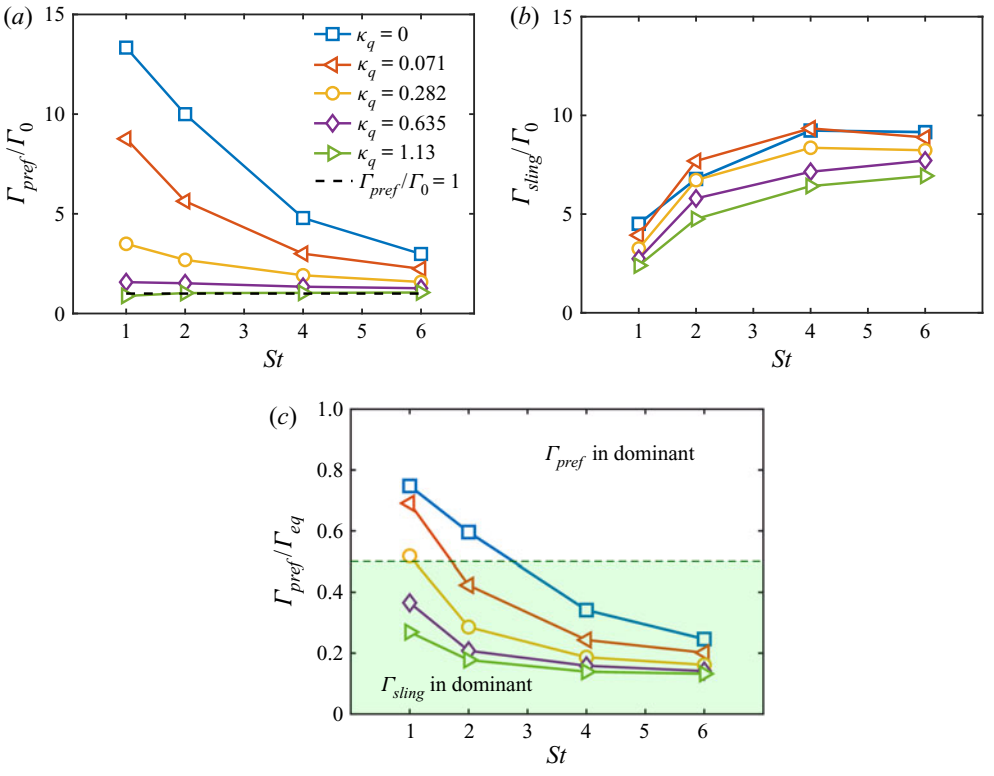

Figure 4. Normalized collision kernel caused by (*a*) preferential concentration Γ_{pref}/Γ_0 and (*b*) the sling effect Γ_{sling}/Γ_0. (*c*) Ratio of the collision contribution by preferential concentration. The horizontal green dash line represents $\Gamma_{pref}/\Gamma_0 = 0.5$. The adhesion parameter Ad equals 0.14 for all cases. The legend in (*a*) also applies to (*b*,*c*).

found to reduce Γ_{pref}/Γ_0 and mitigates the preferential concentration. Specifically, for the strongest charge case ($\kappa_q = 1.13$), the Γ_{pref}/Γ_0 curve almost collapses to a straight line for $\Gamma_{pref}/\Gamma_0 = 1$. This implies that the local particle concentration at contact is close to the average concentration n_0 and only has a limited effect on collision enhancement. Besides, Γ_{pref}/Γ_0 for larger St decreases slower as κ_q increase, because particles with a larger St have a weaker tendency of accumulation and Γ_{pref}/Γ_0 is quite small even for neutral particles.

Figure 4(*b*) illustrates Γ_{sling}/Γ_0 as a function of St for different κ_q. For a fixed κ_q, since the sling becomes more likely to happen for larger particle inertia, Γ_{sling}/Γ_0 shows an increasing dependence on Stokes number. However, Γ_{sling} saturates as St further increases, which could be attributed to the influence of the limited Reynolds number ($Re_\lambda = 74.8$) in this study. As a result, there are no larger-scale motions to further actuate denser particles. For a fixed St, Γ_{sling}/Γ_0 is observed to also drop as κ_q increases, but Γ_{sling}/Γ_0 drops much slower compared to Γ_{pref}/Γ_0, which might be attributed to the large relative velocity between slinging particles. Since the sling effect brings particles together from different regions, the corresponding collisions are more energetic and thus less influenced by the Coulomb repulsion.

We then plot the fraction of the collision contribution due to Γ_{pref} in figure 4(*c*). As can be seen, when St and κ_q are small, the preferential concentration is the dominant mechanism that causes interparticle collisions, whereas the sling effect prevails when

St or κ_q increases. Consequently, as κ_q increases, the major contributor of Γ_{eq} changes from Γ_{pref} to Γ_{sling}, which explains the monotonicity inversion of the dependence on *St* in figure 2(*b*).

3.3. *Effect of Coulomb repulsion on collision velocity*

Apart from the collision frequency, another key issue in particle agglomeration is the collision velocity, which is of importance in determining the agglomerate formation (Chen *et al.* 2019*a*) and the collision-induced breakage (Liu & Hrenya 2018; Chen & Li 2020).

We record the normal collision velocity v_c of each collision event to obtain statistics. Since v_c differs by more than two orders of magnitude, we divide the collision velocity space into ten sub-intervals on a log scale, with $v_{c,i}$ being the median collision velocity of the *i*th sub-interval. Then, all the collision events are classified into the sub-intervals by their colliding velocity. The value of $N_{c,i}(v_{c,i})$ is the number of collision events in the *i*th sub-interval, which is called the grouped collision events number hereafter. From (3.1), the relationship between the collision kernel Γ_{eq} and the grouped collision events number $N_{c,i}(v_{c,i})$ can be written as

$$\Gamma_{eq} = \frac{2}{n_0^2 \cdot \Delta T} \sum_i N_{c,i}(v_{c,i}). \tag{3.5}$$

Figure 5 illustrates the distribution of grouped collision events number $N_{c,i}(v_{c,i})$ of different charge parameter κ_q and *St*. As shown in figure 5(*a*), when particle charge increases, $N_{c,i}(v_{c,i})$ reduces for all $v_{c,i}$. For collisions with small $v_{c,i}$, since the collision kinetic energy is not large enough to overcome the Coulomb repulsion, $N_{c,i}(v_{c,i})$ decreases drastically, while $N_{c,i}(v_{c,i})$ for large $v_{c,i}$ is less affected.

As *St* increases, due to the transition of the dominant mechanism from preferential concentration to the sling effect, the distribution shifts towards the direction of larger $v_{c,i}$ (figure 5*b*,*c*). The collisions of particles with a larger *St* are thus less sensitive to the increases of κ_q.

3.4. *Sticking probability for charged particles*

Once particles collide with each other, it is of great concern to predict whether particles will stick or rebound. For microparticles, the adhesion due to van der Waals force dominates and leads to agglomerate formation (Chen *et al.* 2015; Fang *et al.* 2019). In the previous study of Chen *et al.* (2019*a*), the mean sticking probability θ has been successfully modelled for neutral particles, and the modified adhesion parameter, Ad_n, is proposed to describe the competition between van der Waals adhesion and particle inertia.

Although both translational and rotational motions are considered in the present study, it is the normal contact force that plays a major role in determining the sticking and detachment behaviour. Thus, in this section, the sticking probability is modelled by analysing the momentum equation of particles. We first estimate the relative importance of three forces in a collision process, i.e. the fluid drag force F^{drag}, the normal elastic force F^{ne} and Coulomb force F^E. From (2.20), the ratios between different forces scale as

$$\frac{F^{drag}}{F^{ne}} \sim \frac{1}{Ad \cdot St}, \quad \frac{F^E}{F^{ne}} \sim \frac{\kappa_q}{Ad}. \tag{3.6a,b}$$

By using parameters of typical solid microparticles (table 2), these ratios are much smaller than unity, indicating that the contact force prevails once particles contact each other.

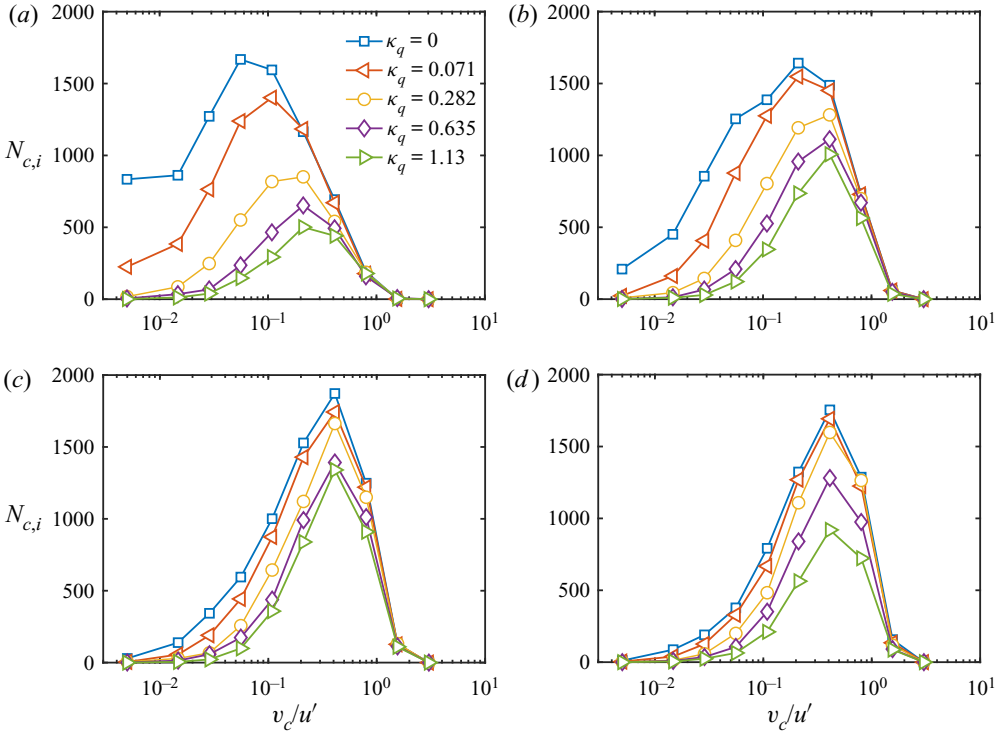

Figure 5. Number of grouped collision events $N_{c,i}$ as a function of collision velocity $v_{c,i}$ for different charge parameters κ_q for (*a*) $St = 1$, (*b*) $St = 2$, (*c*) $St = 4$ and (*d*) $St = 6$. The adhesion parameter Ad equals 0.14. Results are taken over $\Delta T = 12T_e$. The legend in (*a*) applies to all panels.

The effects of the drag force and Coulomb force is thus negligible in collision analysis. The modified adhesion parameter, Ad_n, which is derived from the governing equation for head-on collisions (Chen *et al.* 2019*a*; Chen, Liu & Li 2019*b*), is employed to model the sticking probability

$$Ad_n = \frac{\nu}{\rho_p v_c^2 r_p}. \tag{3.7}$$

In order to find the relation between θ and Ad_n, simulations with different $St(= 1, 2, 4, 6)$ and $Ad(= 11.1, , 22.2)$ for both neutral ($\kappa_q = 0$) and charged particles ($\kappa_q = 1.13$) are run. Again, the collision events in each case are classified into different groups (sub-intervals) by the collision velocity $v_{c,i}$. For each group of collision events, the grouped sticking probability $\theta(v_{c,i})$ is computed by

$$\theta(v_{c,i}) = N_{s,i}(v_{c,i})/N_{c,i}(v_{c,i}). \tag{3.8}$$

Here, $N_{s,i}(v_{c,i})$ is the grouped sticking events number, and $N_{c,i}(v_{c,i})$ is the grouped collision event number. The modified adhesion parameter for each group is then calculated by $Ad_n(v_{c,i}) = \nu/(\rho_p v_{c,i}^2 r_p)$. In the previous study by Chen *et al.* (2019*a*), the mean collision velocity v_{cn} of all the collisions is adopted to define the mean adhesion number, which is later used to model the mean sticking probability. In the present study, by using the median collision velocity $v_{c,i}$ of the ith velocity sub-interval, the modified adhesion parameter $Ad_n(v_{c,i})$ can be used for a more precise prediction of the grouped sticking probability $\theta(v_{c,i})$.

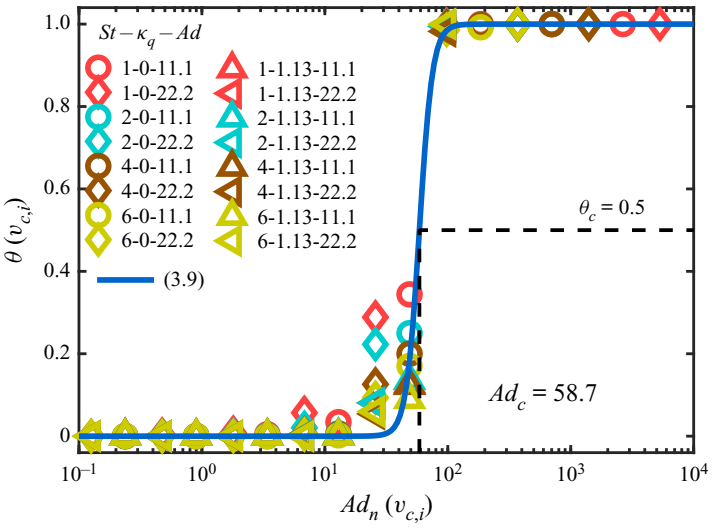

Figure 6. Dependence of the grouped sticking probability $\theta(v_{c,i})$ on the modified adhesion parameter $Ad_n(v_{c,i})$.

To ensure reliable statistics, only the data points $(\theta(v_{c,i}), Ad_n(v_{c,i}))$ with enough collision events $(N_{c,i}(v_{c,i}) \geq 150)$ are shown in figure 6. Despite different St and κ_q, the data collapse on the same curve, which validates our assumption that only $Ad_n(v_{c,i})$ controls this process. When Ad_n is small, the interparticle adhesion is weak. Particles will always rebound after each collision, so the sticking probability $\theta(v_{c,i})$ is zero. As $Ad_n(v_{c,i})$ further increases and exceeds a critical value Ad_C, θ quickly steps up and approaches unity, indicating an adhesion-dominated regime where particles will simply hit and stick. To capture this step-up behaviour, we employ the logistic function for a smooth approximation

$$\theta(Ad_n) = \frac{1}{1 + exp[-a_\theta(\log Ad_n - \log Ad_C)]}. \tag{3.9}$$

Here, Ad_C is the critical value of $Ad_n(v_{c,i})$ that describes where $\theta(v_{c,i})$ steps up, and a_θ characterizes the steepness of this transition. The fitting result is displayed as the blue curve in figure 6, with $a_\theta = 18.71$ and $Ad_C = 58.7$. Equation (3.9) is determined by the collision equation and is independent of the flow conditions. Once we obtain the relative velocity at contact from ghost particle simulation or theoretical derivation, the fitted results can be used empirically to predict the sticking probability.

3.5. *Combined effect of Coulomb repulsion and interparticle adhesion*

In this section, we consider the combined effect of Coulomb repulsion and interparticle adhesion on particle agglomeration. Simulations are run with fixed $Ad = 22.2$ and different St and κ_q. The interparticle adhesion here is strong enough to enable agglomerate formation. In each case, particles will undergo frequent collisions to form non-spherical agglomerates. A snapshot of typical agglomerate structures is given in figure 7(*a*). As time increases, more particles will exist in the form of agglomerates (figure 7*b*), which reduces the particle concentration. As a result, for adhesive particles, the collision kernel calculated by (3.1) will gradually decrease and deviate from the equilibrium collision kernel Γ_{eq} (figure 7*c*).

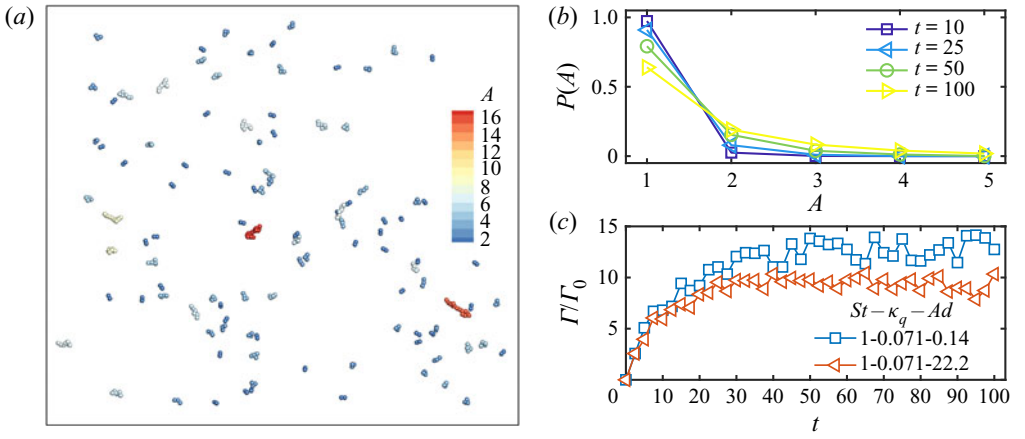

Figure 7. (*a*) Snapshot of typical agglomerate structures. The colour bar represents the number of primary particles in each agglomerate. (*b*) Temporal evolution of the fraction of particles, $P(A)$, existing in the form of agglomerates containing A primary particles for $St = 1$, $\kappa_q = 0.071$ and $Ad = 22.2$. (*c*) Comparison of the temporal evolution of the normalized collision kernel Γ/Γ_0 between $Ad = 0.14/22.2$ for $St = 1$ and $\kappa_q = 0.071$.

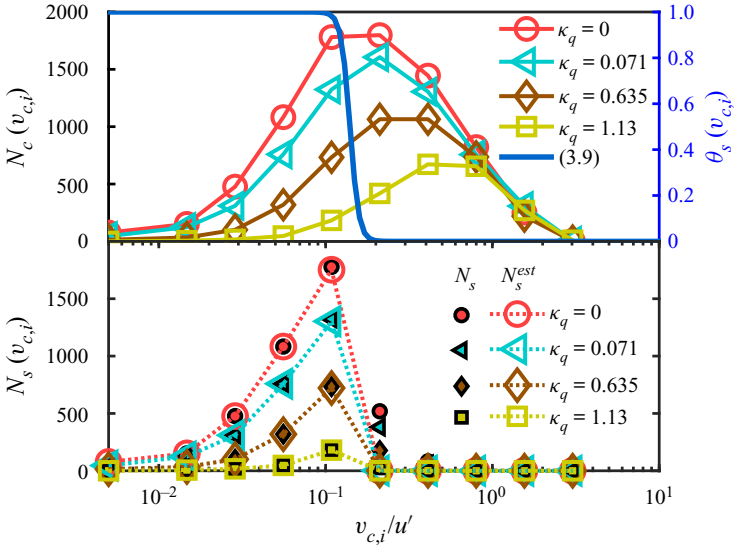

Figure 8. (*a*) Number of grouped collision events $N_{c,i}(v_{c,i})$ for different charge parameters κ_q and $St = 1$. The $\theta(v_{c,i}) - v_{c,i}$ curve is calculated from (3.9). (*b*) Comparison of the grouped sticking events number $N_{s,i}(v_{c,i})$ from simulation and the estimated value $N_{s,i}^{est}(v_{c,i})$ by (3.10) for different charge parameters κ_q and $St = 1$.

We use the number of sticking events instead of the collision kernel to quantify the agglomeration process. The total number of sticking events, N_s, is given by

$$N_s = \sum_i N_{s,i}(v_{c,i}) = \sum_i N_{c,i}(v_{c,i}) \cdot \theta(v_{c,i}). \tag{3.10}$$

Here, $N_{s,i}(v_{c,i})$ is the number of the grouped sticking events with a median collision velocity $v_{c,i}$, which could be further estimated by $N_{s,i}(v_{c,i}) = N_{c,i}(v_{c,i}) \cdot \theta(v_{c,i})$ from (3.8). Figure 8(*a*) illustrates the number of grouped collision events $N_{c,i}(v_{c,i})$ for different

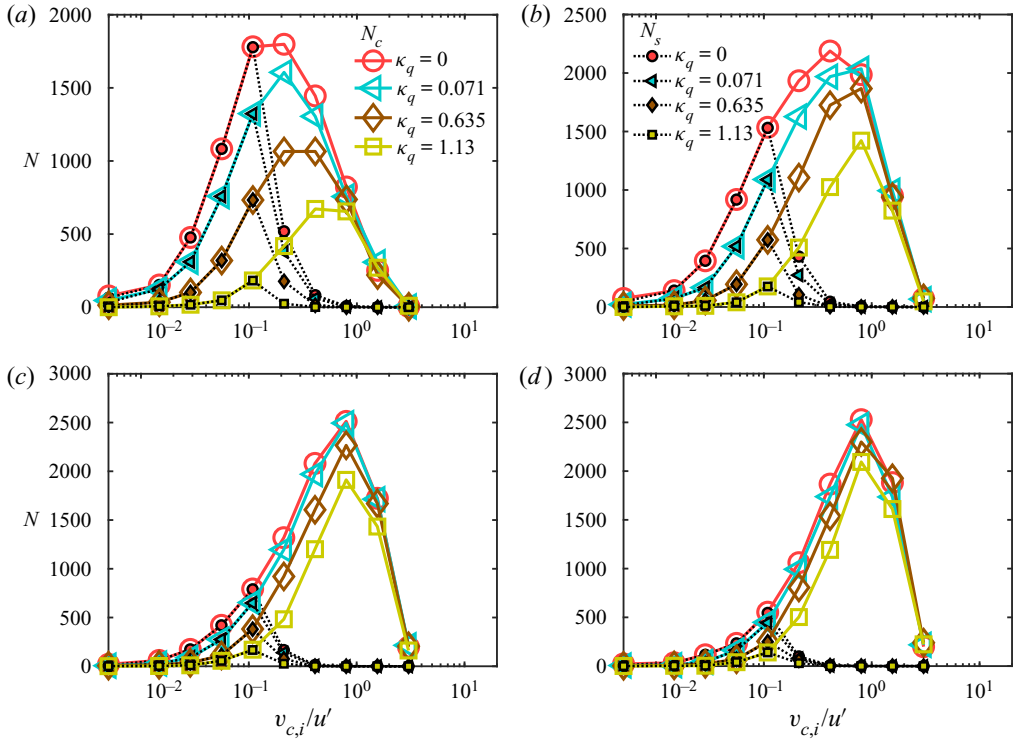

Figure 9. Number of collision events $N_{c,i}$ and sticking events $N_{s,i}$ for different charge parameters κ_q and (*a*) $St = 1$, (*b*) $St = 2$, (*c*) $St = 4$ and (*d*) $St = 6$. Results are taken in a period of time $\Delta T = 100$. $Ad = 22.2$ is fixed for all cases. The legend in (a) applies to all panels.

κ_q with the fixed $St = 1$. The grouped sticking probability $\theta(v_{c,i})$ calculated by (3.9) is also shown as the blue curve (right y-axis). We then estimate the sticking event number $N_{s,i}^{est}(v_{c,i})$ from (3.10) and plot the results as open symbols in figure 8(*b*). In comparison, the number of grouped sticking events $N_{s,i}(v_{c,i})$ directly taken from the simulations is also plotted as closed symbols. The reasonable agreement between $N_{s,i}^{est}(v_{c,i})$ and $N_{s,i}(v_{c,i})$ validates the applicability of (3.9) in charged particle agglomeration. If the physical properties of the particle (e.g. surface energy density, density, radius, etc.) are known *a priori*, one can predict the sticking events number N_s from (3.10) by only conducting simulations for non-adhesive charged particles and then calculating the sticking probability, which will avoid expensive computations resolving interparticle collisions at an ultra-fine collision time step.

To show the combined effect of Coulomb repulsion and interparticle adhesion, figure 9(*a*) plots $N_{c,i}$ and $N_{s,i}$ directly taken for $St = 1$ as open and closed symbols, respectively. For a fixed κ_q, when the collision velocity $v_{c,i}$ is small, $N_{s,i}$ coincides with $N_{c,i}$, indicating that all collision events lead to sticking events. As $v_{c,i}$ further increases and exceeds a critical velocity v_{crit}, the corresponding sticking probability θ decreases to zero. In this case, even though the collision events number $N_{c,i}$ is still large, the number of sticking events $N_{s,i}$ goes down quickly. Therefore, the sticking probability θ acts like a low-pass filter, which only allows particles with a low collision velocity v_c to stick together. For the case shown in figure 9(*a*), taking the critical adhesion parameter $Ad_C = 58.7$ into (3.7) thus yields the critical velocity $v_{crit}/u' = 0.14$. If the interparticle adhesion

becomes stronger, v_{crit} will also increase, resulting in the occurrence of more sticking events. Moreover, when κ_q increases, $N_{c,i}$ decreases significantly for small $v_{c,i}$, which is consistent with the results in figure 5. Since particles with large v_c are more likely to overcome the energy barrier and collide, the effect of Coulomb repulsion is similar to a high-pass filter.

To summarize, when the effects of Coulomb repulsion and interparticle adhesion both exist, collisions with low v_c are suppressed by the Coulomb repulsion, while particles with high v_c will rebound after collisions. Eventually, if one collision leads to sticking, the collision velocity v_c is more likely to lie within a moderate range, which corresponds to the peaks of $N_{s,i}$ curves in figure 9(*a*). This conclusion also applies to different Stokes numbers in figure 9(*b*,*d*). It should be noted that, as St further increases, the collisions become so energetic that most particles will rebound after collisions. As a result, although the number of collision events $N_{c,i}$ for large St are less influenced by Coulomb repulsion, there are still few sticking events that actually contribute to agglomerate formation (figure 9*c*,*d*). Specifically, for different cases with $St = 6$, due to the low sticking probability, almost all the particles ($>99\,\%$) still exist in the form of singlets, doublets and triplets at the end of the simulations ($t = 100$).

Finally, it is of importance to consider the agglomerate structure in our simulation (figure 7*a*), which is closely related to agglomerate migration (Sorensen 2010) and collision dynamics (Chen *et al.* 2019*a*). The gyration radius, R_g, and the fractal dimension, D_f, are often employed to describe the size and compactness of a non-spherical agglomerate. Their definitions are given by

$$R_g = \left(\sum_{i=1}^{A} (\boldsymbol{r}_i - \boldsymbol{r}_C)/A \right)^{1/2}, \tag{3.11}$$

$$A = k_f (R_g/r_p)^{D_f}. \tag{3.12}$$

Here, A is the number of primary particles contained in one agglomerate, $\boldsymbol{r}_C = \sum_{i=1}^{A} \boldsymbol{r}_i/A$ is the mass centre of the agglomerate and k_f is the fractal pre-factor. Figure 10 plots the dimensionless gyration radius R_g/r_p as a function of A for different cases. It can be found that, for a fixed Stokes number, the results for different κ_q collapse on to the same line. This implies that the Coulomb force does not modify the agglomerate structures. This could be attributed to the point-charge model in the present study. Since the charge is assumed to be located at the centroid of particles, the effect of Coulomb force will always be isotropic and repulsive, which does not significantly adjust collision angle or contact point. As a result, the Coulomb force only reduces the agglomeration rate but has no obvious influence on the formed structures. It is worth noting that, when considering the influence of particle polarization, this process could be very different. As two polarized particles approach each other, the dipole force could be attractive in some directions but repulsive in other directions. Consequently, polarized particles tend to stick at certain positions and change the agglomerate structure. This phenomenon is beyond the scope of the present study and left for future investigations.

The fractal dimension D_f and the pre-factor k_f for different St are obtained by fitting (3.12). The fitting parameters are listed in table 3. The fitted fractal dimension D_f is within the range of $1.25 - 1.41$. In turbulent agglomeration, small loose agglomerates are generally formed after initial particle–particle collisions. When these loose agglomerates grow larger, the structures will densify as a result of frequent collisions and restructuring (Selomulya *et al.* 2001; Waldner *et al.* 2005; Ruan, Chen & Li 2020) and the fractal

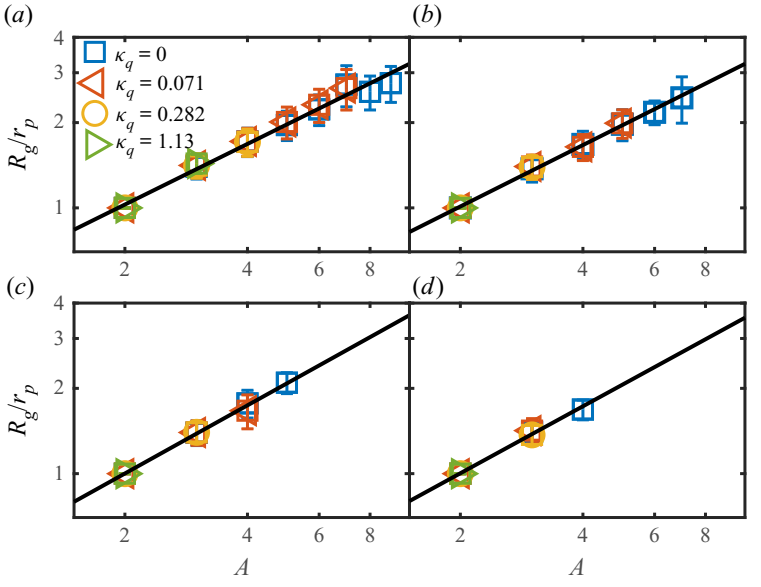

Figure 10. Dimensionless gyration radius R_g/r_p as a function of the number of primary particles A contained in each agglomerate for (*a*) $St = 1$, (*b*) $St = 2$, (*c*) $St = 4$ and (*d*) $St = 6$. Only data points with enough samples are plotted ($n(A) \geq 5$). The legend in (*a*) applies to all panels.

St	1	2	4	6
D_f	1.41 ± 0.08	1.39 ± 0.05	1.25 ± 0.06	1.27 ± 0.10
k_f	0.28 ± 0.02	0.29 ± 0.01	0.30 ± 0.01	0.30 ± 0.01

Table 3. Fitting parameters for agglomerate structure.

dimension will be around 1.7 to 2. In our simulation, however, D_f is quite small, which means the agglomeration is still in the very early stage.

4. Conclusions

By conducting DNS–DEM simulations, the dynamic process of charged particle transport and agglomerate formation is studied in homogeneous isotropic turbulence. The effect of Coulomb repulsion on collision frequency is quantified by calculating the normalized equilibrium collision kernel Γ_{eq}/Γ_0. By decomposing Γ_{eq}/Γ_0, the dominant collision mechanism is found to change from preferential concentration to the sling effect as St and κ_q increase. When particles are at contact, the contact force plays a dominant role, and the modified adhesion parameter Ad_n can successfully predict the sticking probability θ. Besides, due to the combined effect of Coulomb repulsion and interparticle adhesion, particles with a moderate collision velocity are more likely to collide and stick, which largely contributes to particle agglomeration. Furthermore, in our study where the Coulomb force is considered but the effect of higher-order multipoles is omitted, the agglomerate structures formed by charged and neutral particles show no obvious differences.

To understand the impact of Coulomb force from a broader physical picture, it would be beneficial to discuss the relative importance of Coulomb repulsion compared to other

interactions in the process of particle agglomeration. Here, we follow Di Renzo & Urzay (2018) and compare the magnitudes of different velocities caused by turbulence and the Coulomb force. Assuming the characteristic separation distance r_{sep} between like-charged particles varies in the range $(1 \sim 100)\eta$, the electrical migration velocity induced by local particle clusters can be given by

$$u_{el} \sim \frac{n_0 r_{sep}^3 q^2/(4\pi\varepsilon_0 r_{sep}^2)}{3\pi\mu d_p}. \tag{4.1}$$

Taking the parameters from table 2 yields $u_{el}/u_\eta \lesssim 10^{-1}$, which means the present study lies within the weak electrical interaction regime. In this case, Coulomb repulsion does not alter the particle–turbulence interaction on a large scale, but only modifies particle behaviour at a short separation distance (figure 1*a*). The disordered particle distribution can thus be considered amorphous, which is physically relevant for charged solid particles suspended in gaseous turbulence (Lu *et al.* 2010; Di Renzo & Urzay 2018). In comparison, in colloidal systems, the repulsive force could become dominant and repel all the approaching particles. The system thus transits to the crystal state (or the glass state), where the particles assemble in an organized way (Chu & Lin 1994; Fortov *et al.* 2003; Klix, Royall & Tanaka 2010; Gupta *et al.* 2018). As a result, the system is stabilized by the strong repulsion, and the interparticle collision is entirely suppressed.

Another common interaction is the short-range hydrodynamic interaction, or the lubrication force, which is omitted in the present study. The lubrication force is

$$F_{lub} = \frac{3\pi\mu r_p^2}{2h}\left(-\frac{\mathrm{d}h}{\mathrm{d}t}\right). \tag{4.2}$$

Here, μ is the dynamic viscosity of the fluid, r_p is the particle radius and $h = |\boldsymbol{x}_i - \boldsymbol{x}_j| - 2r_p$ is the distance between the surfaces of two particles. The approaching velocity, $-\mathrm{d}h/\mathrm{d}t$, can be estimated by the collision velocity v_c. Based on Marshall (2011), the suggested initial distance and the minimum distance of F_{lub} are given by $h_{max} \sim 0.01 r_p$ and $h_{min} \sim 10^{-4} r_p$. The energy barrier due to the lubrication force can be estimated by

$$\Delta E_{lub} = \int_{h_{min}}^{h_{max}} F_{lub}\,\mathrm{d}h \approx \frac{3\pi\mu r_p^2 v_c}{2}\ln(h_{max}/h_{min}). \tag{4.3}$$

In comparison, the energy barrier caused by the Coulomb force is

$$\Delta E_{Coul} = \frac{q^2}{4\pi\varepsilon_0 d_p}. \tag{4.4}$$

In our simulation, $\mu = 10^{-5}$ Pa · s, $r_p = 10$ μm, $v_c \sim (10^{-2} - 1)$ m s^{-1}. If a particle's charging density is of the order of 10 μC m^{-2} (or $q \sim 10^{-14}$ C), the energy barriers can be estimated as $\Delta E_{lub} \sim (10^{-16} - 10^{-14})J$ and $\Delta E_{Coul} \sim (10^{-14} - 10^{-13})J$. Thus, compared to Coulomb interaction, the short-range hydrodynamic interaction has a weaker impact. But under certain conditions of weak particle charge and large collision velocity, the short-range hydrodynamic interaction could become more important. In the present study, we focus on the impact of Coulomb repulsion, so the effect of the short-range hydrodynamic interaction is intentionally neglected.

In addition, as discussed in § 3.4, the contact force is found to play an essential role when particles contact each other. Here, we adopt the normal contact force as a

typical measure of the contact interactions, which equals $F_{ne} = 4F_C[(a/a_0)^3 - (a/a_0)^{3/2}]$ (§ 2.2.4). The Coulomb force between two contacting particles is $F_{Coul} = q^2/(4\pi\varepsilon_0|\boldsymbol{x}_1 - \boldsymbol{x}_2|^2)$ under the point-charge assumption. For physical relevant parameters given in table 2, the ratio $F_{ne}/F_{Coul} \sim O(10)$. Thus, the normal contact force prevails once interparticle collision happens.

Based on our results, there are several interesting directions for future investigations. First, in this study, we focus on the early-stage agglomeration process. In this stage, most particles exist in the form of singlets or small agglomerates. Particle behaviour still resembles that of single particles. If the agglomeration goes on, agglomerates will continue to grow larger. How these large agglomerates react to the turbulence is still unclear and remains to be resolved. Second, the present study adopts the point-charge model to include electrostatic interactions, and some important electrical effects are neglected. First of all, the charge transfer during frequent collisions (McCarty & Whitesides 2008; Jin & Marshall 2017; Kolehmainen *et al.* 2017) and the electrical breakdown (Matsuyama & Yamamoto 1995; Soh *et al.* 2012) will significantly change the particle charge distribution and further affect the Coulomb force. In addition to the point-charge assumption, when particles are close to each other, the induced higher-order multipoles could have a significant impact on the particle behaviour. Consequently, particles could form chain-like structures, experience stronger clustering and probably encounter runaway growth (Ivelev *et al.* 2002; Liu *et al.* 2010; Lee *et al.* 2015; Kolehmainen *et al.* 2018).

Moreover, the present study is limited to the same Reynolds number ($Re_\lambda = 74.8$). For neutral particles, the increase of Re_λ has been reported to significantly affect both the spatial clustering and the relative velocity, and therefore enhances interparticle collisions (Wang *et al.* 2000; Ireland *et al.* 2016*a*,*b*; Dou *et al.* 2018). Hence, how charged particle dynamics could be modified in a broader range of Re_λ may be worth pursuing in future studies.

Acknowledgements. We are grateful to Professor C. Sun at Tsinghua University, Professor R. Ni at Johns Hopkins University and Professor Y. Jin at Institute of Theoretical Physics, Chinese Academy of Sciences for fruitful discussions.

Funding. S.Q.L. acknowledges support from the National Natural Science Foundation of China (No. 51725601) and the NSFC-DFG Joint Program, China (No. 51761135126).

Declaration of interests. The authors report no conflict of interest.

Author ORCIDs.
Xuan Ruan http://orcid.org/0000-0002-7890-5390;
Sheng Chen http://orcid.org/0000-0003-0006-973X;
Shuiqing Li http://orcid.org/0000-0003-4443-5316.

References

Agasthya, L., Picardo, J., Ravichandran, S., Govindarajan, S. & Ray, S. 2019 Understanding droplet collisions through a model flow: insight from a Burgers vortex. *Phys. Rev.* E **99**, 063107.

Almohammed, N. & Breuer, M. 2016 Modeling and simulation of agglomeration in turbulent particle-laden flows: a comparison between energy-based and momentum-based agglomeration models. *Powder Technol.* **294**, 373–402.

Balachandar, S. & Eaton, J. 2009 Turbulent dispersed multiphase flow. *Annu. Rev. Fluid Mech.* **42**, 111–133.

Balkovsky, E., Falkovich, G. & Fouxon, A. 2001 Intermittent distribution of inertial particles in turbulent flows. *Phy. Rev. Lett.* **86**, 2790–2793.

Balme, M. & Greeley, R. 2006 Dust devils on Earth and Mars. *Rev. Geophys.* **44**, RG3003.

Barnes, J. & Hut, P. 1986 A hierarchical O(NlogN) force-calculation algorithm. *Nature* **324**, 446–449.

BEC, J., BIFERALE, L., CENCINI, M., LANOTTE, A., MUSACCHIO, S. & TOSCHI, F. 2007 Heavy particle concentration in turbulence at dissipative and inertial scales. *Phys. Rev. Lett.* **98**, 084502.

BEC, J., HOMANN, H. & RAY, S. 2014 Gravity-driven enhancement of heavy particle clustering in turbulent flow. *Phys. Rev. Lett.* **112**, 184501.

BEC, J., MUSACCHIO, S. & RAY, S. 2013 Sticky elastic collisions. *Phys. Rev.* E **87**, 063013.

BEC, J., RAY, S., SAW, E. & HOMANN, H. 2016 Abrupt growth of large aggregates by correlated coalescences in turbulent flow. *Phys. Rev.* E **93**, 031102(R).

BEWLEY, G., SAW, E. & BODENSCHARTZ, E. 2013 Observation of the sling effect. *New J. Phys.* **15**, 083051.

BHATNAGAR, A., GUSTAVSSON, K., MEHLIG, B. & MITRA, D. 2018*a* Relative velocities in bidisperse turbulent aerosols: simulations and theory. *Phys. Rev.* E **98**, 063107.

BHATNAGAR, A., GUSTAVSSON, K. & MITRA, D. 2018*b* Statistics of the relative velocity of particles in turbulent flows: monodisperse particles. *Phys. Rev.* E **97**, 023105.

BOUTSIKAKIS, A., FEDE, P., PEDRONO, A. & SIMONIN, O. 2020 Numerical simulations of short- and long-range interaction forces in turbulent particle-laden gas flows. *Flow Turbul. Combust.* **105**, 989–1015.

BREUER, M. & ALMOHAMMED, N. 2015 Modelling and simulation of particle agglomeration in turbulent flows using a hard-sphere model with deterministic collision detection and enhanced structure models. *Intl J. Multiphase Flow* **73**, 171–206.

CALZAVARINI, E., CENCINI, M., LOHSE, D. & TOSCHI, F. 2008*b* Quantifying turbulence-induced segregation of inertial particles. *Phys. Rev. Lett.* **101**, 084504.

CALZAVARINI, E., KERSCHER, M., LOHSE, D. & TOSCHI, F. 2008*a* Dimensionality and morphology of particle and bubble clusters in turbulent flow. *J. Fluid Mech.* **607**, 13–24.

CHEN, S. & LI, S. 2020 Collision-induced breakage of agglomerates in homogeneous isotropic turbulence laden with adhesive particles. *J. Fluid Mech.* **902**, A28.

CHEN, S., LI, S., LIU, W. & MAKSE, H. 2016*a* Effect of long-rang repulsive Coulomb interactions on packing structure of adhesive particles. *Soft Matt.* **12**, 1836–1846.

CHEN, S., LI, S. & MARSHALL, J. 2019*a* Exponential scaling in early-stage agglomeration of adhesive particles in turbulence. *Phys. Rev. Fluids* **4**, 024304.

CHEN, S., LI, S. & YANG, M. 2015 Sticking/rebound criterion for collisions of small adhesive particles: effects of impact parameter and particle size. *Powder Technol.* **274**, 431–440.

CHEN, S., LIU, W. & LI, S. 2016*b* Effect of long-range electrostatic repulsion on pore clogging during microfiltration. *Phys. Rev.* E **84**, 063108.

CHEN, S., LIU, W. & LI, S. 2019*b* A fast adhesive discrete element method for random packings of fine particles. *Chem. Engng Sci.* **193**, 336–345.

CHU, J. & LIN, I. 1994 Direct observation of Coulomb crystals and liquids in strongly coupled RF dusty plasmas. *Phys. Rev. Lett.* **72**, 4009.

CHUN, J., KOCH, D., RANI, S., AHLUWALIA, A. & COLLINS, L. 2005 Clustering of aerosol particles in isotropic turbulence. *J. Fluid Mech.* **536**, 219–251.

DI FELICE, R. 1994 The voidage function for fluid-particle interaction systems. *Intl J. Multiphase Flow* **20**, 153–159.

DI RENZO, M. & URZAY, J. 2018 Aerodynamic generation of electric fields in turbulence laden with charged inertial particles. *Nature Commun.* **9**, 1676.

DIZAJI, F. & MARSHALL, J. 2017 On the significance of two-way coupling in simulation of turbulent particle agglomeration. *Powder Technol.* **318**, 83–94.

DOU, Z., BRAGG, A., HAMMOND, A., LIANG, Z., COLLINS, L. & MENG, H. 2018 Effect of Reynolds number and Stoke number on particle-pair relative velocity in isotropic turbulence: a systematic experimental study. *J. Fluid Mech.* **839**, 271–292.

EATON, J. & FESSLER, J. 1994 Preferential concentration of particles by turbulence. *Intl J. Multiphase Flow* **20**, 169–209.

FALKOVICH, G., FOUXON, A. & STEPANOV, M. 2002 Acceleration of rain initiation by cloud turbulence. *Nature* **419**, 151–154.

FALKOVICH, G., GAWEDZKI, K. & VERGASSOLA, M. 2001 Particles and fields in fluid turbulence. *Rev. Mod. Phys.* **73**, 913–975.

FALKOCIVH, G. & PUMIR, A. 2007 Sling effect in collisions or water droplets in turbulent clouds. *J. Atmos. Sci.* **64**, 4497–4505.

FANG, Z., WANG, H., ZHANG, Y., WEI, M., WU, X. & SUN, L. 2019 A finite element method (FEM) study on adhesive particle-wall normal collision. *J. Aero. Sci.* **134**, 80–94.

FORTOV, V., *et al.* 2003 Transport of microparticles in weakly ionized gas-discharge plasmas under microgravity conditions. *Phys. Rev. Lett.* **90**, 245005.

GILBERT, J., LANE, S., SPARKS, R. & KOYAGUCHI, T. 1991 Charge measurements on particle fallout from a volcanic plume. *Nature* **349**, 598–600.

GOTO, S. & VASSILICOS, J. 2008 Sweep-stick mechanism of heavy particle clustering in fluid turbulence. *Phys. Rev. Lett.* **100**, 054503.

GRABOWSKI, W. & WANG, L. 2013 Growth of cloud droplets in a turbulent environment. *Annu. Rev. Fluid Mech.* **45**, 293–324.

GUPTA, M., CHAUDHURI, P., BEC, J. & RAY, S. 2018 Turbulent route to two-dimensional soft crystals. arXiv:1812.06487v1.

GUSTAVSSON, K. & MEHLIG, B. 2014 Relative velocities of inertial particles in turbulent aerosols. *J. Turbul.* **15**, 34–69.

IRELAND, P., BRAGG, A. & COLLINS, L. 2016*a* The effect of Reynolds number on inertial particle dynamics in isotropic turbulence: part 1. Simulations without gravitational effects. *J. Fluid Mech.* **796**, 617–658.

IRELAND, P., BRAGG, A. & COLLINS, L. 2016*b* The effect of Reynolds number on inertial particle dynamics in isotropic turbulence: part 2. Simulations witht gravitational effects. *J. Fluid Mech.* **796**, 659–711.

ISRAELACHVILI, J. 2011 *Intermolecular and Surface Forces*. Academic Press.

IVELEV, A., MORFILL, G. & KONOPKA, U. 2002 Coagulation of charged microparticles in neutral gas and charge-induced gel transition. *Phys. Rev. Lett.* **89**, 195502.

JAMES, M. & RAY, S. 2017 Enhanced droplet collision rates and impact velocities in turbulent flows: the effect of poly-dispersity and transient phases. *Sci. Rep.* **7**, 122231.

JAWOREK, A., MARCHEWICZ, A., SOBCZYK, A., KRUPA, A. & CZECH, T. 2018 Two-stage electrostatic precipitators for the reduction of PM2.5 particle emission. *Prog. Energy Combust. Sci.* **67**, 206–233.

JAYARAM, R., JIE, Y., ZHAO, L. & ANDERSSON, H. 2020 Clustering of inertial spheres in evolving Taylor-Green vortex flow. *Phys. Fluids* **32**, 043306.

JIN, X. & MARSHALL, J. 2017 The role of fluid turbulence on contact electrification of suspended particles. *J. Electrostat.* **87**, 217–227.

JOHNSON, K., KENDALL, K. & ROBERTS, A. 1971 Surface energy and the contact of elastic solids. *Proc. R. Soc. Lond.* A **324**, 301–313.

JONES, T. 1995 *Electromechanics of Particles*. Cambridge University Press.

DE JONG, J., SALAZAR, J., WOODWARD, S., COLLINS, L. & MENG, H. 2010 Measurement of inertial particle clustering and relative velocity statistics in isotropic turbulence using holographic imaging. *Intl J. Multiphase Flow* **36**, 324–332.

KARNIK, A. & SHRIMPTON, J. 2012 Mitigation of preferential concentration of small inertial particles in stationary isotropic turbulence using electrical and gravitational body force. *Phys. Fluids* **24**, 073301.

KLIX, C., ROYALL, C. & TANAKA, H. 2010 Structural and dynamical features of multiple metastable glassy states in a colloidal system with competing interactions. *Phys. Rev. Lett.* **104**, 165702.

KOLEHMAINEN, J., OZEL, A., BOYCE, C.M. & SUNDARESAN, S. 2017 Triboelectric charging of monodisperse particles in fluidized beds. *AIChE J.* **63**, 1872–1891.

KOLEHMAINEN, J., OZZEL, A., GU, Y., SHINBROT, T. & SUNDARESAN, S. 2018 Effect of polarization on particle-laden flows. *Phys. Rev. Lett.* **121**, 124603.

LEE, V., WAITUKAITIS, S., MISKIN, M. & JAEGER, H. 2015 Direct observation of particle interactions and clustering in charged granular streams. *Nature Phys.* **11**, 733–737.

LI, S. & MARSHALL, J. 2007 Discrete element simulation of micro-particle deposition on a cylindrical fiber in an array. *J. Aero. Sci.* **38**, 1031–1046.

LI, S., MARSHALL, J., LIU, G. & YAO, Q. 2011 Adhesive particulate flow: the discrete-element method and its application in energy and environmental engineering. *Prog. Energy Combust. Sci.* **37**, 622–668.

LIU, P. & HRENYA, C. 2018 Cluster-induced deagglomeration in dilute gravity-driven gas-solid flows of cohesive grains. *Phys. Rev. Lett.* **121**, 238001.

LIU, G., MARSHALL, J., LI, S. & YAO, Q. 2010 Discrete-element method for particle capture by a body in an electrostatic field. *Intl J. Numer. Meth. Engng* **84**, 1589–1612.

LU, J., NORDSIEK, H., SAW, E. & SHAW, R. 2010 Clustering of charged inertial particles in turbulence. *Phys. Rev. Lett.* **104**, 184505.

LU, J. & SHAW, R. 2015 Charged particle dynamics in turbulence: theory and direct numerical simulations. *Phys. Fluids* **27**, 065111.

MARCHIOLI, C. & SOLDATI, A. 2002 Mechanisms for particle transfer and segregation in a turbulent boundary layer. *J. Fluid Mech.* **468**, 283–315.

MARSHALL, J. 2009 Discrete-element modeling of particulate aerosol flows. *J. Comput. Phys.* **228**, 1541–1561.

MARSHALL, J. 2011 Viscous damping force during head-on collision of two spherical particles. *Phys. Fluids* **23**, 013305.

MARSHALL, J. & LI, S. 2014 *Adhesive Particle Flow: A Discrete-Element Approach*. Cambridge University Press.

MATHAI, V., CALZAVARINI, E., BRONS, J., SUN, C. & LOHSE, D. 2016 Microbubbles and microspheres are not truthful tracers of turbulent acceleration. *Phys. Rev. Lett.* **117**, 024501.
MATHAI, V., LOHSE, D. & SUN, C. 2020 Bubbly and buoyant particle-laden turbulent flows. *Annu. Rev. Condens. Matter Phys.* **11**, 529–559.
MATSUYAMA, T. & YAMAMOTO, H. 1995 Charge relaxation process dominates contact charging of a particle in atmospheric conditions. *J. Phys.* D*: Appl. Phys.* **28**, 2418–2423.
MAXEY, M. 1987 The gravitational settling of aerosol particles in homogeneous turbulence and random flow fields. *J. Fluid Mech.* **174**, 441–465.
MCCARTY, L. & WHITESIDES, G. 2008 Electrostatic charging due to separation of ions at interfaces: contact electrification of ionic electrets. *Angew. Chem. Intl Ed.* **47**, 2188–2207.
MONCHAUX, R., BOURGOIN, M. & CARTELLIER, A. 2010 Preferential concentration of heavy particles: a Voronoï analysis. *Phys. Fluids* **22**, 103304.
ONISHI, R., MATSUDA, K. & TAKAHASHI, K. 2015 Lagrangian tracking simulation of droplet growth in turbulence – turbulence enhancement of autoconversion rate. *J. Atmos. Sci.* **72**, 2591–1607.
PÄHTZ, T., HERR,AMM, H. & SHINBROT, T. 2010 Why do particle clouds generate electric charges? *Nature Phys.* **6**, 364–368.
PERRIN, V. & JONKER, H. 2014 Preferred location of droplet in turbulent flows. *Phys. Rev.* E **89**, 033005.
PERRIN, V. & JONKER, H. 2016 Effect of the eigenvalues of the velocity gradient tensor on particle collisions. *J. Fluid Mech.* **792**, 36–49.
PICARDO, J., AGASTHYA, L., GOVINDARAJAN, R. & RAY, S. 2019 Flow structures govern particle collisions in turbulence. *Phys. Rev. Fluids* **4**, 032601(R).
PUMIR, A. & WILKINSON, M. 2016 Collisional aggregation due to turbulence. *Annu. Rev. Condens. Matter Phys.* **7**, 141–70.
READE, W. & COLLINS, L. 2000 Effect of preferential concentration on turbulent collision rates. *Phys. Fluids* **12**, 2530–2540.
RUAN, X., CHEN, S. & LI, S. 2020 Structural evolution and breakage of dense agglomerates in shear flow and Taylor-Green vortex. *Chem. Engng Sci.* **211**, 115261.
RUBINOV, S.I. & KELLER, J.B. 1961 The transverse force on a spinning sphere moving in a viscous fluid. *J. Fluid Mech.* **11**, 447–459.
SAFFMAN, P. 1965 The lift on a small sphere in a slow shear flow. *J. Fluid Mech.* **22**, 385–400.
SAFFMAN, P. & TURNER, J. 1956 On the collision of drops in turbulent clouds. *J. Fluid Mech.* **1**, 16–30.
SALAZAR, J., DE JONG, J., CAO, L., WOODWARD, S., MENG, H. & COLLINS, L. 2008 Experimental and numerical investigation of inertial particle clustering in isotropic turbulence. *J. Fluid Mech.* **600**, 245–256.
SALMON, J.K. & WARREN, M.S. 1994 Skeletons from the tree code closet. *J. Comput. Phys.* **111**, 136–155.
SAW, E., BEWLEY, G., BODENSCHATZ, E., RAY, S. & BEC, J. 2014 Extreme fluctuations of the relative velocities between droplets in turbulent airflow. *Phys. Fluids* **26**, 111702.
SAW, E., SHAW, R., AYYALASOMAYAJULA, S., CHUANG, P. & GYLFASON, A. 2008 Inertial clustering of particles in high-Reynolds-number turbulence. *Phys. Rev. Lett.* **100**, 21501.
SELOMULYA, C., AMAL, R., BUSHELL, G. & WAITE, T. 2001 Evidence of shear rate dependence on restructuring and breakup of latex aggregates. *J. Colloid Interface Sci.* **236**, 67–77.
SHAW, R. 2003 Particle-turbulence interactions in atmospheric clouds. *Annu. Rev. Fluid Mech.* **35**, 183–227.
SHRIMPTON, J. & YULE, A. 1999 Characterisation of charged hydrocarbon sprays for application in combustion systems. *Exp. Fluids* **26**, 460–469.
SMOLUCHOWSKI, M. 1916 Versuch einer mathematischen Theorie der Koagulationskinetik kolloider Lösungen. *Z. Phys. Chem.* **92U** (1), 129–168.
SOH, S., KWOK, S., LIU, H. & WHITESIDES, G. 2012 Contact de-electrification of electrostatically charged polymers. *J. Am. Chem. Soc.* **134**, 20151–20159.
SORENSEN, C.M. 2010 The mobility of fractal aggregates: a review. *Aero. Sci. Technol.* **45**, 765–779.
SQUIRE, K. & EATON, J. 1991 Preferential concentration of particles by turbulence. *Phys. Fluids* A **3**, 1169–1178.
SÜMER, B. & SITTI, M. 2008 Rolling and spinning friction characterization of fine particles using lateral force microscopy based contact pushing. *J. Adhes. Sci. Technol.* **22**, 481–506.
SUN, J., BATTAGLIA, F. & SUBRAMANIAM, S. 2006 Dynamics and structures of segregation in a dense, vibrating granular bed. *Phys. Rev.* E **74**, 061307.
SUNDARAM, S. & COLLINS, L. 1997 Collision statistics in an isotropic particle-laden turbulent suspension. Part 1. Direct numerical simulations. *J. Fluid Mech.* **335**, 75–109.
TAGAWA, Y., MERCADO, J., PRAKASH, V., CALZAVARINI, E., SUN, C. & LOHSE, D. 2012 Three-dimensional Lagrangian Voronoï analysis for clustering of particles and bubbles in turbulence. *J. Fluid Mech.* **693**, 201–215.

TOSCHI, F. & BODENSCHATZ, E. 2009 Lagrandian properties of particles in turbulence. *Annu. Rev. Fluid Mech.* **41**, 375–404.

TRYGGVASON, G., SCARDOVELLI, R. & ZALESKI, S. 2011 *Direct Numerical Simulations of Gas-Solid Multiphase Flows*. Cambridge University Press.

TSUJI, Y., TANAKA, T. & ISHIDA, T. 1992 Lagrangian numerical simulation of plug flow of cohesionless particles in a horizontal pipe. *Powder Technol.* **71**, 239–250.

VOßKUHLE, M., PUMIR, A., LÉVÊQUE, E. & WILKINSON, M. 2014 Prevalence of the sling effect for enhancing collision rates in turbulent suspensions. *J. Fluid Mech.* **749**, 841–852.

WALDNER, M., SEFCIK, J., SOOS, M. & MORBIDELLI, M. 2005 Initial growth kinetics and structure of colloidal aggregates in a turbulent coagulator. *Powder Technol.* **156**, 226–234.

WANG, L. & MAXEY, M. 1993 Settling velocity and concentration distribution of heavy particles in homogeneous isotropic turbulence. *J. Fluid Mech.* **256**, 27–68.

WANG, L., WEXLER, A. & ZHOU, Y. 2000 Statistical mechanical description and modelling of turbulent collision of inertia particles. *J. Fluid Mech.* **415**, 117–153.

WILKINSON, M. & MEHLIG, B. 2005 Caustics in turbulent aerosols. *Europhys. Lett.* **71**, 186–192.

WILKINSON, M., MEHLIG, B. & BEZUGLYY, V. 2006 Caustic activation of rain showers. *Phys. Rev. Lett.* **97**, 048501.

YAO, Y. & CAPECELATRO, J. 2018 Competition between drag and Coulomb interactions in turbulent particle-laden flows using a coupled-fluid-Ewald-summation based approach. *Phys. Rev. Fluids* **3**, 034301.

ZHANG, H. & ZHOU, H. 2020 Reconstructing the electrical structure of dust storms from locally observed electric field data. *Nature Commun.* **11**, 5072.

ZHAO, L., ANDERSSON, H. & GILLISSEN, J. 2010 Turbulence modulation and drag reduction by spherical particles. *Phys. Fluids* **22**, 081702.